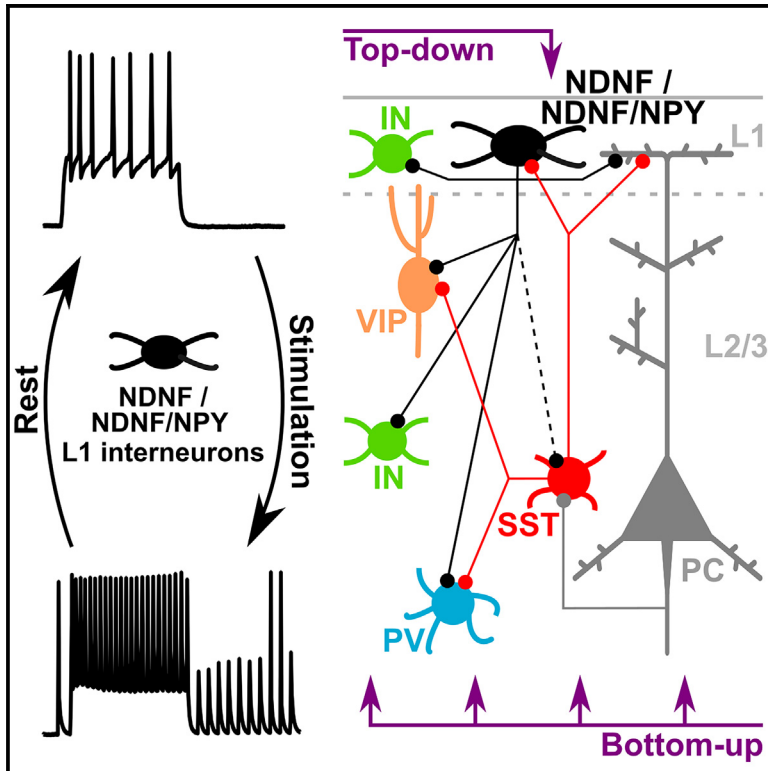


Layer 1 NDNF interneurons are specialized top-down master regulators of cortical circuits

Graphical abstract



Authors

Jan Hartung, Anna Schroeder,
Rodrigo Alejandro Pérez Vázquez,
Rogier B. Poorthuis, Johannes J. Letzkus

Correspondence

jan.hartung@physiologie.uni-freiburg.de
(J.H.),
johannes.letzkus@physiologie.
uni-freiburg.de (J.J.L.)

In brief

Neocortical layer 1 is a unique site for the processing of top-down information related to memory and perception. Using a selective marker for layer 1 interneurons, Hartung et al. reveal that these understudied cells act as a master regulator of superficial neocortex and can undergo a dedicated, long-lasting activity mode switch.

Highlights

- NDNF interneurons in neocortical layer 1 provide pervasive inhibition of other interneurons
- NDNF interneurons comprise two physiologically distinct subgroups
- They can switch from integration to generation of signals by a specialized activity mode
- This activity mode is associated with a long-lasting transition of physiological state



Article

Layer 1 NDNF interneurons are specialized top-down master regulators of cortical circuits

Jan Hartung,^{1,2,5,*} Anna Schroeder,¹ Rodrigo Alejandro Pérez Vázquez,¹ Rogier B. Poorthuis,³ and Johannes J. Letzkus^{1,2,4,6,*}

¹Institute for Physiology, Faculty of Medicine, University of Freiburg, 79108 Freiburg, Germany

²BrainLinks-BrainTools, IMBIT (Institute for Machine-Brain Interfacing Technology), University of Freiburg, Georges-Köhler-Allee 201, 79110 Freiburg, Germany

³Department of Translational Neuroscience, UMC Utrecht Brain Center, Utrecht University, Utrecht, the Netherlands

⁴Center for Basics in NeuroModulation (NeuroModul Basics), University of Freiburg, 79106 Freiburg, Germany

⁵X (formerly Twitter): @JanHartung_

⁶Lead contact

*Correspondence: jan.hartung@physiologie.uni-freiburg.de (J.H.), johannes.letzkus@physiologie.uni-freiburg.de (J.J.L.)
<https://doi.org/10.1016/j.celrep.2024.114212>

SUMMARY

Diverse types of inhibitory interneurons (INs) impart computational power and flexibility to neocortical circuits. Whereas markers for different IN types in cortical layers 2–6 (L2–L6) have been instrumental for generating a wealth of functional insights, only the recent identification of a selective marker (neuron-derived neurotrophic factor [NDNF]) has opened comparable opportunities for INs in L1 (L1INs). However, at present we know very little about the connectivity of NDNF L1INs with other IN types, their input-output conversion, and the existence of potential NDNF L1IN subtypes. Here, we report pervasive inhibition of L2/3 INs (including parvalbumin INs and vasoactive intestinal peptide INs) by NDNF L1INs. Intersectional genetics revealed similar physiology and connectivity in the NDNF L1IN subpopulation co-expressing neuropeptide Y. Finally, NDNF L1INs prominently and selectively engage in persistent firing, a physiological hallmark disconnecting their output from the current input. Collectively, our work therefore identifies NDNF L1INs as specialized master regulators of superficial neocortex according to their pervasive top-down afferents.

INTRODUCTION

Neocortical layer 1 (L1) stands apart from all other layers in several respects: it is the thinnest of all layers and the only molecular layer, being mostly composed of the distal dendrites of deeper pyramidal cells (PCs) and interneurons (INs) as well as extensive long-range afferents from a variety of sources.^{1–4} These pathways transmit internally generated top-down information that encodes previous experiences and current goals and is essential for a range of higher brain functions including memory and perception.^{5–8} In addition, L1 contains a small population of resident INs, which control apical PC dendrites^{9–12} and are thus in a prime position to control integration of top-down information in the local circuit.

While research on layer 1 INs (L1INs) lagged for a long time behind the work on deeper IN types with known markers (strongly focused on parvalbumin [PV], somatostatin [SST], and vasoactive intestinal peptide [VIP] expressing populations),^{13–15} the recent identification of neuron-derived neurotrophic factor (NDNF) as a genetic marker selectively labeling approximately two-thirds of L1INs (NDNF L1INs) in both mouse and human neocortex has now opened the door to a similarly rigorous functional dissection of these cells.^{16–20} To date, this work has revealed that the sensory responses of NDNF L1INs are exquisitely

sensitive to previous experience¹⁶ and arousal,¹⁸ in line with the host of top-down afferents these cells receive, including from the higher-order thalamus^{7,16–18} as well as cortical^{16,18,20} and subcortical areas,^{16,18,20} such as the zona incerta^{8,16,18} and the cholinergic system.²¹ These data therefore identify NDNF L1INs as central actuators of long-range top-down input in the local circuit.¹⁹ Intriguingly, the second local type of inhibition targeting L1 is provided by SST Martinotti cells that are predominantly driven by local recurrent excitation and in consequence also display very different, often opposite *in vivo* encoding attributes.^{13–15,19,22–24} Whereas both NDNF L1INs and SSTINs control distal apical PC dendrites in L1,^{13–17,23–25} and SSTINs are moreover known to connect broadly to different IN types in L2–L6,^{23,24,26} a similarly detailed understanding of the output connectivity of NDNF L1INs is currently lacking. Since this precludes a precise definition of the circuit function of NDNF L1INs, we address these issues here. Moreover, virtually all IN types defined by a single marker gene are thought to comprise functionally distinct subtypes.²⁷ Following a recent landmark study,²⁸ we therefore validate and employ an intersectional genetic approach²⁹ to selectively target the subpopulation of NDNF L1INs that co-express neuropeptide Y (NPY). Finally, we provide a detailed characterization of the physiological attributes of NDNF L1INs and reveal that the majority of these neurons



robustly and selectively engage in persistent firing (pF), a distinct activity mode that can uncouple their action potential output from external stimulation for protracted time periods.^{30–34}

RESULTS

Pervasive inhibition of L2/3 IN types by NDNF L1INs

In addition to the properties and somatodendritic location of inhibition on PCs, a primary factor determining the circuit function of an IN type are its outputs to other INs. IN-IN interactions are instrumental for generating neuronal oscillations,^{13–15} can gate learning and memory retrieval through disinhibition,^{8,35–37} and may fundamentally add computational power to the network, since IN-IN interactions are particularly pervasive in human neocortex.³⁸ Importantly, IN types vary widely in their IN targets and connection specificity: whereas PVINs supply little inhibition to other IN types and VIPINs rather selectively connect to SSTINs, SSTINs themselves provide strong input to all other populations, including NDNF L1INs.^{9,16,26} However, while it has been established that NDNF L1INs contact the distal apical dendrites of PCs and control dendritic calcium electrogenesis there,^{16–18} their output wiring with respect to other IN types remains incompletely understood.

To define the IN-specific output wiring of NDNF L1INs and systematically compare the properties of these connections, we focused on the auditory cortex, where these cells and unidentified L1INs have been linked to learning and memory as a high-level function.^{1,16,19,37,39} Employing selective *Ndnf-ires-cre-ERT2* and *Ndnf-ires-FlpO* mouse lines we previously generated¹⁶ enabled us to optogenetically probe the outputs of NDNF L1INs to different L2/3 IN types in acute slices from adult animals (Figure 1A, age 78–242 days, median 125 days). To obtain data under standardized conditions and ensure comparability to previous work,¹⁶ we calibrated the irradiance for each optogenetic activator to evoke approximately one action potential (AP) per light pulse in a train of four stimulations delivered at 1 Hz in NDNF L1INs using whole-cell patch-clamp recordings (Figures 1B and 1C). To probe the connectivity from NDNF L1INs to VIPINs, we crossed *Ndnf-ires-FlpO* mice with *VIP-cre* mice⁴⁰ and injected them with a mix of adeno-associated viral vectors (AAVs), leading to *flp*-dependent expression of the activator ChrimsonR for optogenetic activation and *cre*-dependent expression of the fluorescent marker *tdTomato* for targeting of VIPINs. This revealed robust connectivity, with 10 out of 12 tested VIPINs displaying inhibitory postsynaptic currents (IPSCs) that crossed the third standard deviation of baseline and were therefore scored as connected (Figures 1D–1H; see STAR Methods for details). These IPSCs were characterized by slow rise and decay times (Figures 1I–1K) and displayed significant short-term depression (Figures 1L and 1M). In conclusion, these data uncover a connection from NDNF L1INs to VIPINs that displays several of the hallmarks previously described for their inputs to PCs.^{16–18}

Next, we performed analogous experiments on PVINs. For identification of these cells, we utilized recently developed viral approaches, since these are compatible with the intersectional targeting of NDNF/NPY L1INs employed below. PVINs (Figure 1A, $n = 20$) were thus identified either by the PVIN-specific

AAV-S5E2-*tdTomato*⁴¹ or by IN-specific AAV-mDlx-mRuby⁴² together with a maximal sustained evoked firing rate exceeding 150 Hz (Figure S1), a known hallmark of these cells within cortical circuits.⁴³ The latter approach, furthermore, yielded a dataset on non-fast-spiking INs (non-FS INs, $n = 14$) for comparison. PVINs receive inputs from NDNF L1INs with high probability (Figure 1F, 17/20). Whereas none of the attributes of single IPSCs differed between PVINs and VIPINs (Figures 1G–1K), we observed stronger short-term depression in NDNF L1IN inputs to PVINs compared to VIPINs (Figures 1L and 1M), suggesting that inhibition of VIPINs is temporally more sustained. Together, these results therefore demonstrate that NDNF L1INs inhibit both VIPINs and PVINs as well as further unidentified L2/3 INs, with high probability. Together with the established connectivity to other L1INs and PC distal dendrites,^{16–18} this suggests that NDNF L1INs serve as master regulators of superficial neocortex.

SSTINs are a second highly connected type of INs that have been suggested to function as master regulators.^{9,16,26} To understand the interrelation between these two master regulators, we reanalyzed data on NDNF L1IN inputs to L2/3 SSTINs that was previously acquired in the lab using the same experimental approach and irradiance calibration strategy.¹⁶ These datasets contain both connected and unconnected recordings and thus reflect the combined effect of connection probability and strength. This revealed that NDNF L1IN inputs to SSTINs are weaker than to either VIPINs or PVINs (Figures 1G and 1H), suggesting that the SSTIN master regulator is not strongly controlled by the NDNF L1IN master. In conclusion, these results unpack the logic of L1-led IN-IN interactions recruited by top-down afferents^{1–4} and contrast it with SSTIN-dependent circuit regulation controlled by local recurrent excitation.^{13–15,19,22–24}

NDNF L1INs comprise two physiologically distinct clusters

Given the central role of NDNF L1INs for controlling superficial circuits of neocortex, we next asked whether these cells may comprise functionally distinct subtypes, as has been shown for the general L1IN population in both mouse and human neocortex.^{9,19,21,28,44–46} As a first step toward addressing this question, we performed whole-cell recordings on a comprehensive set of genetically targeted NDNF L1INs (Figures 2A–2C, $n = 145$) and used a standard current step protocol to exhaustively define 14 of their intrinsic physiological properties. In particular, we extracted the following parameters: AP onset time, amplitude, threshold, half-width, and maximal slope; AP afterhyperpolarization (AHP) amplitude and half-width; interspike interval accommodation and variability; membrane potential; input resistance; time constant; amplitude of a depolarizing hump in the last subthreshold step; and voltage sag (Table S1). This revealed heterogeneity in a number of properties including AP onset time and threshold, voltage sag, or resting membrane potential (Figures 2C and S2A). Since all recordings were performed in current clamp, we additionally confirmed that between-cell variability in resting membrane potential does not negatively impact our measurements of the voltage sag by correlating the sag fraction measured in both current clamp and voltage clamp in the same cell in a subset of cells (Figures S2B–S2D, Pearson's $r = 0.94$, $p = 4.1 \times 10^{-5}$).

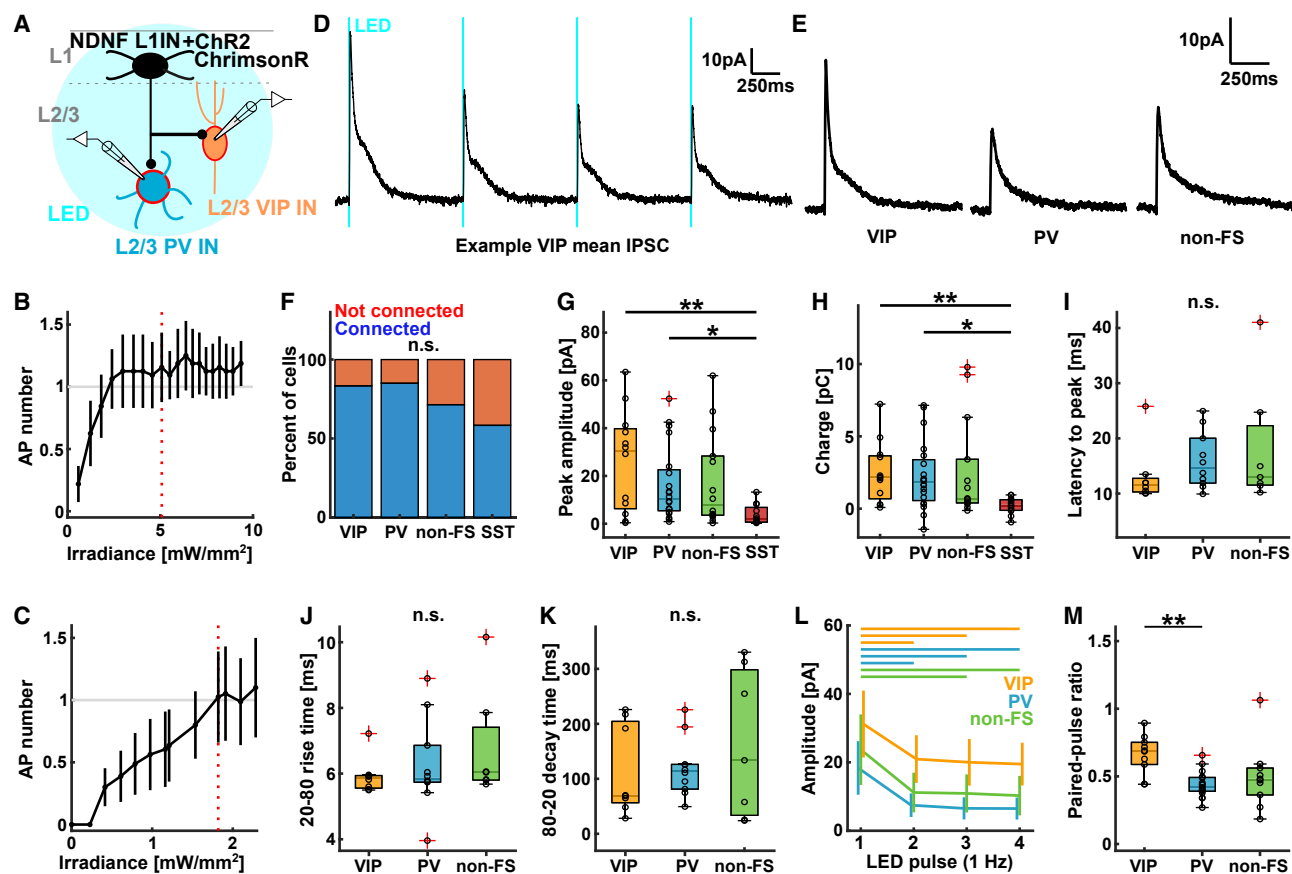


Figure 1. Pervasive inhibition of L2/3 IN types by NDNF L1INs

(A) Experimental design.

(B and C) Calibration of irradiance to evoke on average one action potential per LED pulse in NDNF L1INs expressing DIO-ChR2-EYFP in *Ndnf-ires-cre-ERT2* mice ($n = 8$ cells) (B) or fDIO-ChrimsonR in *Ndnf-ires-FlpO* mice ($n = 5$ cells) (C). Red line indicates chosen irradiance.

(D) Example trace of IPSCs recorded in an L2/3 VIPIN (average of 15 trials).

(E) Grand average traces of all connected INs by type ($n_{VIP} = 10$, $n_{PV} = 17$, $n_{nonFS} = 10$).

(F) Proportion of connected INs by type ($n_{VIP} = 10/12$, $n_{PV} = 17/20$, $n_{nonFS} = 10/14$, $n_{SST} = 7/12$; chi-squared test $p = 0.33$).

(G) IPSC peak amplitude ($n_{VIP} = 12$, $n_{PV} = 20$, $n_{nonFS} = 14$, $n_{SST} = 12$). Kruskal-Wallis test with post hoc Dunn's procedure: $p_{group} = 0.0077$, $p_{VIP-PV} = 0.98$, $p_{VIP-nonFS} = 0.87$, $p_{VIP-SST} = 0.0081$, $p_{PV-nonFS} = 1$, $p_{PV-SST} = 0.026$, $p_{nonFS-SST} = 0.13$.

(H) IPSC charge ($n_{VIP} = 12$, $n_{PV} = 20$, $n_{nonFS} = 14$, $n_{SST} = 12$). Kruskal-Wallis test with post hoc Dunn's procedure: $p_{group} = 0.005$, $p_{VIP-PV} = 1$, $p_{VIP-nonFS} = 0.94$, $p_{VIP-SST} = 0.0085$, $p_{PV-nonFS} = 1$, $p_{PV-SST} = 0.11$, $p_{nonFS-SST} = 0.087$.

(I–K) IPSC kinetics ($n_{VIP} = 8$, $n_{PV} = 10$, $n_{nonFS} = 7$). Latency to peak amplitude (I), 20–80 rise time (J), and 80–20 decay time (K). Kruskal-Wallis test: $p_{peak} = 0.31$, $p_{rise} = 0.44$, $p_{decay} = 0.75$. Note that for analysis of IPSC kinetics, signals with an amplitude <10 pA were excluded due to poor signal-to-noise ratio.

(L) Short-term depression of NDNF L1IN-elicited IPSCs ($n_{VIP} = 10$, $n_{PV} = 17$, $n_{nonFS} = 10$). Data displayed as mean \pm SEM. Bars on top indicate significant differences. Within-cell-type Friedman test with post hoc Dunn's procedure: VIP: $p_{group} = 5.8e-4$, $p_{12} = 0.019$, $p_{13} = 0.033$, $p_{14} = 4e-4$, $p_{23} = 1$, $p_{24} = 0.88$, $p_{34} = 0.78$. PV: $p_{group} = 6.9e-8$, $p_{12} = 0.0086$, $p_{13} = 5.3e-6$, $p_{14} = 3e-7$, $p_{23} = 0.41$, $p_{24} = 0.14$, $p_{34} = 1$. non-FS: $p_{group} = 2.3e-4$, $p_{12} = 0.14$, $p_{13} = 0.006$, $p_{14} = 1.9e-4$, $p_{23} = 0.88$, $p_{24} = 0.3$, $p_{34} = 0.95$. (M) Paired-pulse ratio ($2^{nd}/1^{st}$ IPSC amplitude) by cell type ($n_{VIP} = 10$, $n_{PV} = 17$, $n_{nonFS} = 10$). Kruskal-Wallis test $p = 0.0028$, post hoc Dunn's procedure: $p_{VIP-PV} = 0.0019$, $p_{VIP-nonFS} = 0.075$, $p_{PV-nonFS} = 0.74$.

Red crosses in boxplots represent outliers and were included in the analysis. See also Figure S1.

Notably, a small proportion of NDNF L1INs displayed burst firing upon spike onset, and some cells showed rebound APs after hyperpolarization (Figures S2E and S2F).

To test whether these properties vary independently or alternatively may define electrophysiological subtypes of NDNF L1INs, we subjected the data to an unsupervised clustering approach (Figures 2D–2H). Individual parameters were normalized in order to equilibrate their contribution (see STAR Methods). Importantly, four independent approaches for evalua-

tion of optimal cluster number converged on a local optimum of two main clusters for this approach (Figures S3A–S3D), suggesting that NDNF L1INs are best described by two physiological clusters. Post hoc comparison revealed that the clusters differ in 9 out of 14 properties, suggesting robust separation. To further analyze the degree of cluster separation, we performed principal component analysis (PCA) (Figures 2E and S3E). This revealed that cluster 2 (81/145 cells) is composed of cells in which a late AP onset typically co-occurs with higher AP thresholds, longer

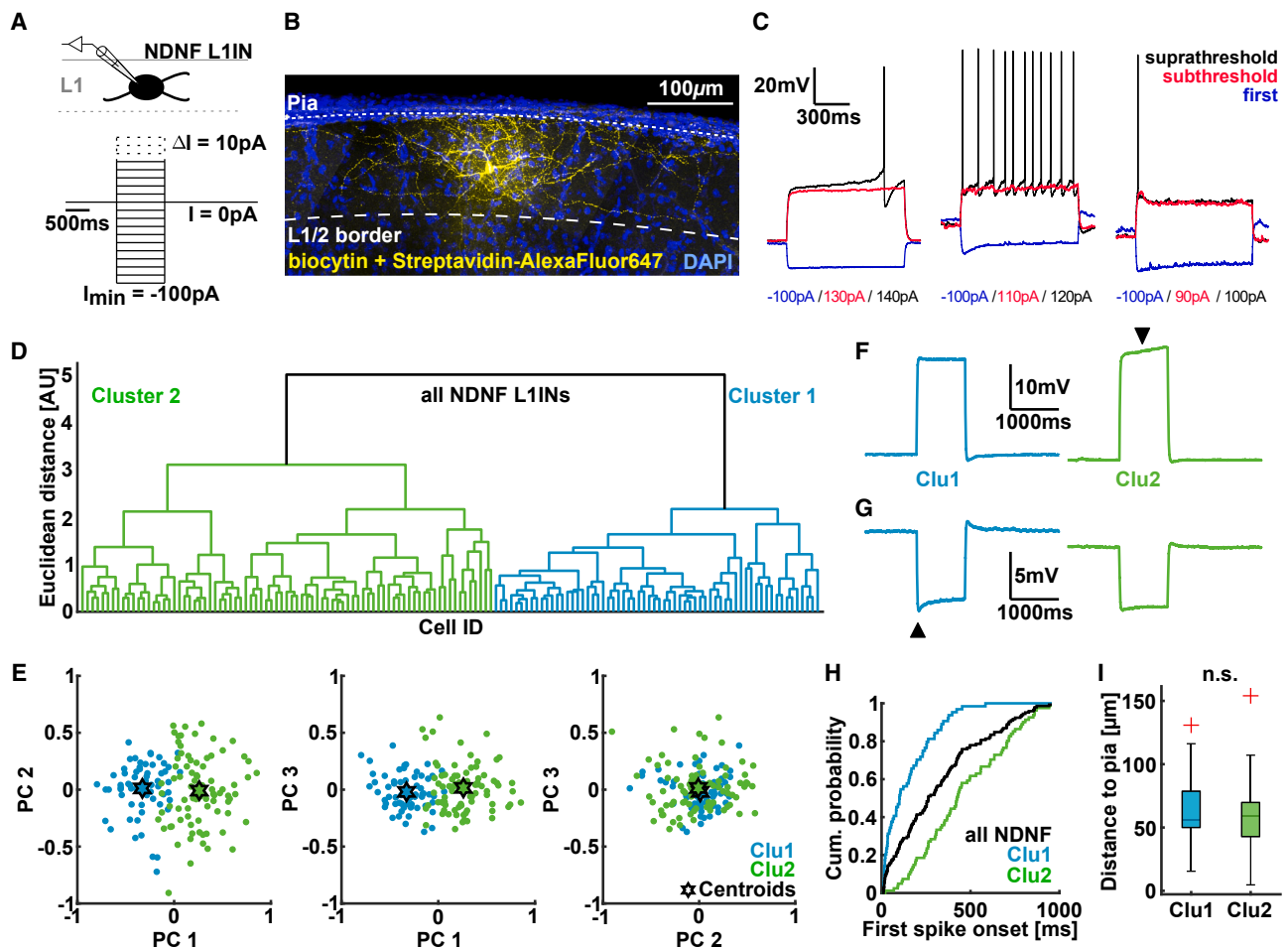


Figure 2. NDNF L1INs comprise two physiologically distinct clusters

(A) Experimental design.
 (B) Example histology of a recorded NDNF L1IN filled with biocytin. Scale bar, 100 μ m.
 (C) Example traces of the first (blue) and last (red) subthreshold, and the first suprathreshold (black) step. Left: late-spiking IN with depolarizing ramp. Center: non-late-spiking IN with pronounced voltage sag in first step. Right: non-late-spiking IN with depolarizing hump in last subthreshold step.
 (D) Ward's unsupervised clustering of recorded intrinsic electrophysiological properties of NDNF L1INs ($n = 145$) reveals two clusters ($n_{\text{Cluster1}} = 64$, $n_{\text{Cluster2}} = 81$). Cells for which one or more intrinsic properties could not be measured were excluded.
 (E) Principal component projection illustrating cluster separation ($n_{\text{Clu1}} = 64$, $n_{\text{Clu2}} = 81$, color code corresponds to clusters obtained from D).
 (F) Average traces of the last subthreshold step for the two clusters. Black arrow indicates depolarizing ramp in cluster 2 ($n_{\text{Clu1}} = 64$, $n_{\text{Clu2}} = 81$).
 (G) Average traces of the step used for voltage-sag measurement (black arrow, $n_{\text{Clu1}} = 64$, $n_{\text{Clu2}} = 81$).
 (H) Cumulative distribution of first AP onset by cluster identity ($n_{\text{Clu1}} = 64$, $n_{\text{Clu2}} = 81$).
 (I) Distance to pia of recorded NDNF INs by cluster identity ($n_{\text{Clu1}} = 50$, $n_{\text{Clu2}} = 41$). Wilcoxon rank-sum test $p = 0.48$. Red crosses in boxplots represent outliers and were included in the analysis.
 See also [Figures S2](#) and [S3](#).

AP half-widths, and larger AHPs. In contrast, cells in cluster 1 (64/145 cells) display early AP onsets together with larger AP amplitudes and slopes, larger voltage sags, and depolarizing humps ([Figures 2F–2H](#) and [S3F–S3H](#)). Finally, we tested whether cells in the two clusters differ in their distance from the pia mater but found very similar distributions ([Figure 2I](#)). Together, these data indicate that adult auditory cortex NDNF L1INs can be described as two well-separated clusters based on physiology. The presence of a late-spiking phenotype with low sag fraction and depolarizing ramp that is reminiscent of previous reports from neurogliaform cells (NGFCs),^{21,44,47} and a second type

characterized by early spike onset and large sag fraction and depolarizing hump, is consistent with previous work on the general L1IN population^{9,19,21,44–46} as well as a dissection specifically of NDNF L1INs²⁸ and Lamp5-MET1INs, a class of interneurons largely overlapping with NDNF L1INs.⁴⁸

Functional attributes of NDNF L1INs co-expressing NPY

The fact that NDNF L1INs comprise two physiologically defined clusters may suggest the presence of distinct functional subtypes^{20,28} but is equally compatible with a single type whose properties vary along a continuum.^{46,48} To disambiguate these

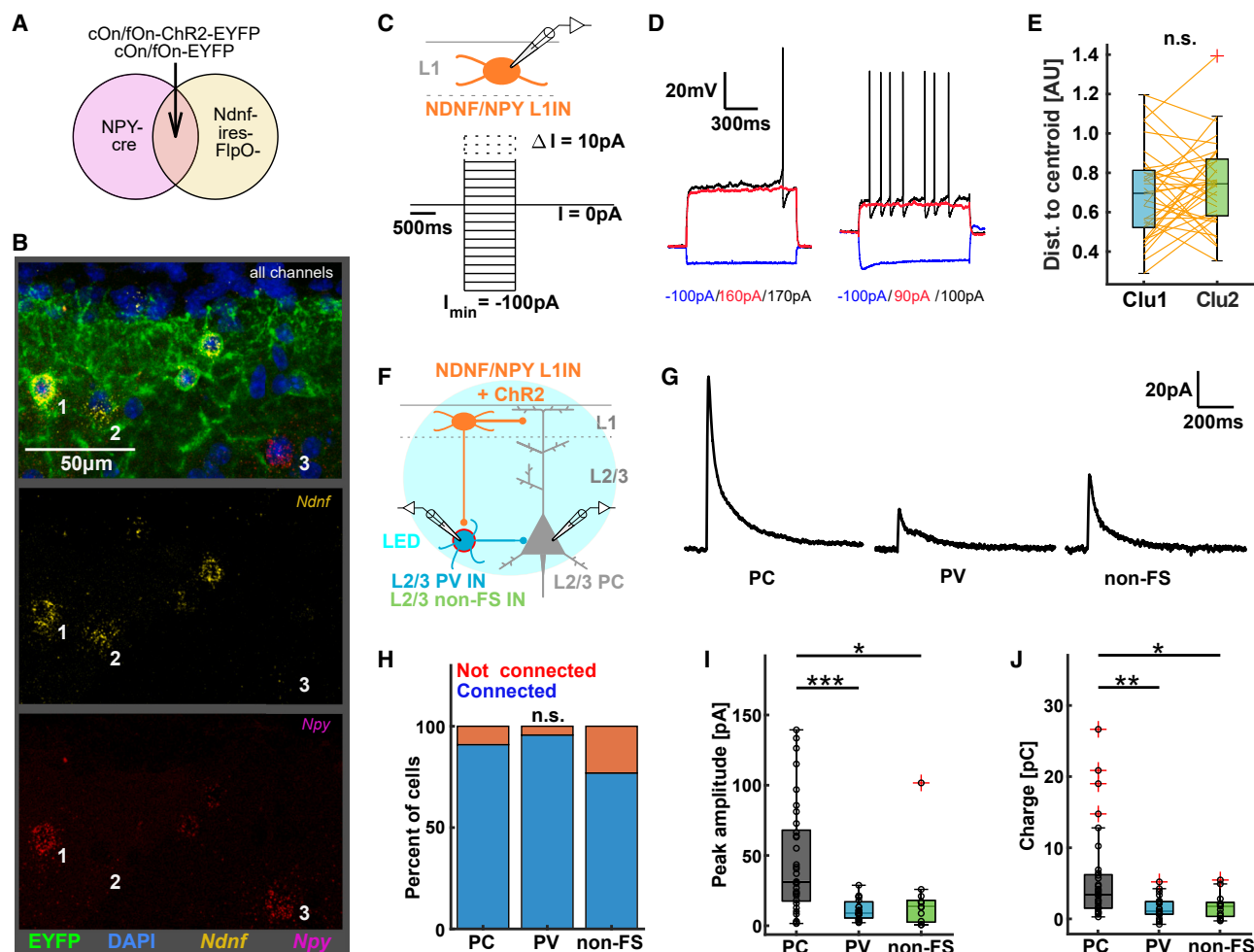


Figure 3. Functional attributes of NDNF L1INs co-expressing NPY

(A) Intersectional targeting approach. Npy-cre mice were crossed with Ndnf-ires-FlpO mice and injected with AAV-cOn/fOn-ChR2-EYFP or AAV-cOn/fOn-EYFP, targeting the NDNF L1IN population co-expressing Npy.

(B) Example histology of intersectional EYFP (green) expression combined with *in situ* hybridization of *Ndnf* (yellow) and *Npy* (magenta) mRNA. Cell 1 co-expresses *Ndnf* and *Npy* mRNA and is EYFP positive. Cell2 is labeled for *Ndnf* but not *Npy* mRNA and is EYFP negative. Cell 3 is labeled for *Npy* but not *Ndnf* mRNA and is EYFP negative.

(C) Experimental design to measure electrophysiological properties (same approach as in Figure 2).

(D) Example traces of the first (blue) and last (red) subthreshold, and the first suprathreshold (black) step. Left: late-spiking NDNF/NPY L1IN. Right: non-late-spiking NDNF/NPY L1IN with voltage sag in first step.

(E) Pairwise comparison of distances of individual NDNF/NPY L1INs ($n = 36$) from the NDNF L1IN cluster centroids in full intrinsic property space. Wilcoxon signed rank test $p = 0.29$.

(F) Experimental approach to measure connectivity from NDNF/NPY L1INs to L2/3. cOn/fOn-ChR2-EYFP was expressed in NDNF/NPY INs in Ndnf-ires-FlpO::Npy-cre mice while in L2/3, PCs were identified morphologically and PVINs and non-FS INs by expression of AAV-MDlx-mRuby and AAV-S5E2-tdTomato.

(G) Grand average traces of all connected cells by type ($n_{PC} = 30$, $n_{PV} = 22$, $n_{nonFS} = 10$).

(H) Percentage of connected cells by cell type ($n_{PC} = 30/33$, $n_{PV} = 22/23$, $n_{nonFS} = 10/13$). Chi-squared test $p = 0.19$.

(I) Peak IPSC amplitude ($n_{PC} = 33$, $n_{PV} = 23$, $n_{nonFS} = 13$). Kruskal-Wallis test with Dunn's post hoc procedure: $p_{\text{group}} = 8.8\text{e-}5$, $p_{PC-PV} = 1.8\text{e-}4$, $p_{PC-nonFS} = 0.012$, $p_{PV-nonFS} = 0.96$.

(J) IPSC charge ($n_{PC} = 33$, $n_{PV} = 23$, $n_{nonFS} = 13$). Kruskal-Wallis test with Dunn's post hoc procedure: $p_{\text{group}} = 9.1\text{e-}4$, $p_{PC-PV} = 0.0016$, $p_{PC-nonFS} = 0.037$, $p_{PV-nonFS} = 0.98$.

Red crosses in boxplots represent outliers and were included in the analysis. See also Figures S4–S7.

alternatives, we asked whether NDNF L1INs co-expressing the marker neuropeptide Y (NDNF/NPY L1INs) may represent a functional subtype, as has recently been suggested in juvenile somatosensory cortex.²⁸ To this end, we employed an intersec-

tional genetic targeting approach²⁹ (Figures 3A and S4A). Validation by *in situ* hybridization demonstrates that these vectors can be used for accurate targeting of NDNF/NPY L1INs (Figures 3B and S4).

We next asked whether NDNF/NPY L1INs may correspond to one of the physiological clusters we identified above (Figure 2). To this end, we targeted these cells by whole-cell patch-clamp recordings ($n = 36$) and recorded their attributes as in Figure 2 (Figure 3C). This revealed both late-spiking and non-late-spiking neurons, similar to the overall population of NDNF L1INs (Figure 3D). Moreover, when taking into account the first three components of a PCA, we found that the centroids of NDNF/NPY L1IN data were much closer to the centroid of the overall NDNF L1IN population than to centroids of either cluster (Figures S5A–S5C). Similarly, directly comparing NDNF/NPY IN distances to the two clusters in a pairwise manner using the full intrinsic property space revealed no significant differences (Figures 3E, S5D, S5E, and S6). Similar results were also obtained when splitting the NDNF L1IN data into three clusters (not shown). Taken together, these results indicate that NDNF/NPY L1INs do not correspond to one of the previously identified NDNF L1IN clusters but are instead most likely identical to the overall NDNF L1IN population with regard to their intrinsic physiological attributes.

NDNF/NPY L1INs may also differ from the overall NDNF L1IN population in their output connectivity as a second, functionally relevant organizational feature. To address this, we optogenetically activated NDNF/NPY L1INs and recorded the postsynaptic responses in L2/3 PCs, PVINs (identified by AAV-S5E2-tdTomato⁴¹), and non-FS INs (identified by AAV-mDlx-mRuby⁴²; Figures 3F and S7). To ensure comparability to previous datasets, we calibrated the irradiance to evoke approximately one AP per light pulse in a train of four stimulations delivered at 1 Hz (Figure S7A). This uncovered similarly high connectivity to all neuron types tested (Figures 3G and 3H). In contrast, IPSCs in PCs displayed larger amplitudes and charge transfer than in either PVINs or non-FS INs (Figures 3I and 3J), in line with similar results for the overall NDNF L1IN population.^{16,17} Also consistent with our observations for NDNF L1INs, no differences in IPSC kinetics were detected between the three target cell types (Figures S7B–S7D), and IPSCs also displayed similarly pronounced short-term depression in all three target cell types (Figures S7E and S7F). Moreover, sequential recordings from a PC and a PVIN in close spatial proximity in the same slice revealed larger IPSC amplitudes in PCs, ruling out technical caveats as the source of the observed difference (Figure S7G). Finally, we addressed the contribution of GABA_B receptors as a well-described hallmark of inhibition from NDNF L1INs.^{16,49} The selective antagonist CGP-55845 (3 μ M) caused a robust reduction in the decay times of IPSCs evoked by NDNF/NPY L1IN stimulation in PCs and PVINs (Figures S7H and S7I), indicating the presence of a GABA_B receptor component. Taken together, our data indicate that both NDNF/NPY and NDNF INs pervasively inhibit neocortical L2/3, including PCs as well as PV and non-FS INs. In combination with the similar physiology, we therefore did not observe relevant differences between NDNF L1INs with and without expression of NPY.

A specialized activity mode in NDNF L1INs

Our results so far identify NDNF L1INs as physiologically heterogeneous master regulators of superficial neocortex according to their pervasive top-down afferents.^{1,2,8,16–18} We next asked

whether additional hallmarks may set these cells apart from other IN types. Indeed, we frequently observed continued, autonomous AP firing after the offset of the depolarizing current injection in NDNF L1INs (Figures 4A–4C, turquoise arrows). This pF has been described for hippocampal and cortical NGFCs^{30–33} and is a fundamental attribute, since it can effectively uncouple the activity of NDNF L1INs from ongoing synaptic input. Consistent with this being a dedicated activity mode, evoked APs and persistent APs displayed clear kinetic differences, with persistent APs being characterized by a clear deceleration in the upstroke (Figures 4D and 4E). Moreover, episodes of pF comprised both full APs and spikelets with lower amplitudes, whereas spikelets were not observed during evoked firing (Figures 4C, 4D, and S8A). Importantly, pF was not caused by poor cell health or recording quality, since it was typically confined to a single or a few inter-step intervals and since it completely reversed during the course of the recording (Figure S8B, median ectopic AP number: before pF 0 APs, during pF 112 APs, after pF 0 APs). Of note, in extreme cases pF could last for several minutes (Figure S9).

Is pF a unique capacity of NDNF L1INs? To address this, we classified a large number of recordings from different neuron types. Based on the recent report that pF can also occur as sporadic events,³¹ we defined a conservative criterion of five APs occurring ectopically (without current injection) in the complete recording to score a neuron as capable for pF (pF+, Figure S8C). This revealed that approximately two-thirds of NDNF L1INs display pF (Figure 4F, NDNF INs 79/128), whereas the proportion was much lower in PVINs (13/69), non-FS INs (4/44), and PCs (4/34). Moreover, the number of ectopic APs observed in NDNF L1INs vastly exceeded that in other neuronal types (Figure S8D, median number of ectopic APs: NDNF L1INs 63 APs; PVINs: 0 APs; non-FS INs: 0 APs; PCs: 0 APs). Importantly, we observed no significant differences in either the number of cells displaying pF or the number of ectopic APs between NDNF L1INs and NDNF/NPY INs, nor between the two physiologically defined NDNF L1IN clusters (Figures 4F and S8D), demonstrating that pF is a property of NDNF L1INs in general. In line with this, we could identify only two physiological properties within the NDNF L1IN population, the resting membrane potential and the membrane time constant, that differed between cells that showed pF and those that did not show pF (Figure S10). In contrast, all other parameters, including those most strongly contributing to the variance in the NDNF L1IN population (Figures S3F–S3H), displayed no statistically significant differences.

Within the NDNF L1IN population, both the number of inter-step intervals with pF and the maximum number of ectopic APs per inter-step interval varied widely (Figure S8E). Moreover, a small proportion of recorded NDNF L1INs displayed persistent activity before the onset of evoked APs (Figure S8F). Together, this indicates that the capacity for pF is quite variable within the NDNF L1IN population and that some INs are more prone to it than others. A second parameter that notably varied is the proportion of spikelets among ectopic events. After defining a formal criterion to separate persistent APs and spikelets (Figure S8G), we found that 44% of NDNF L1INs displayed only persistent APs, 49% showed both persistent APs and spikelets, and 7%

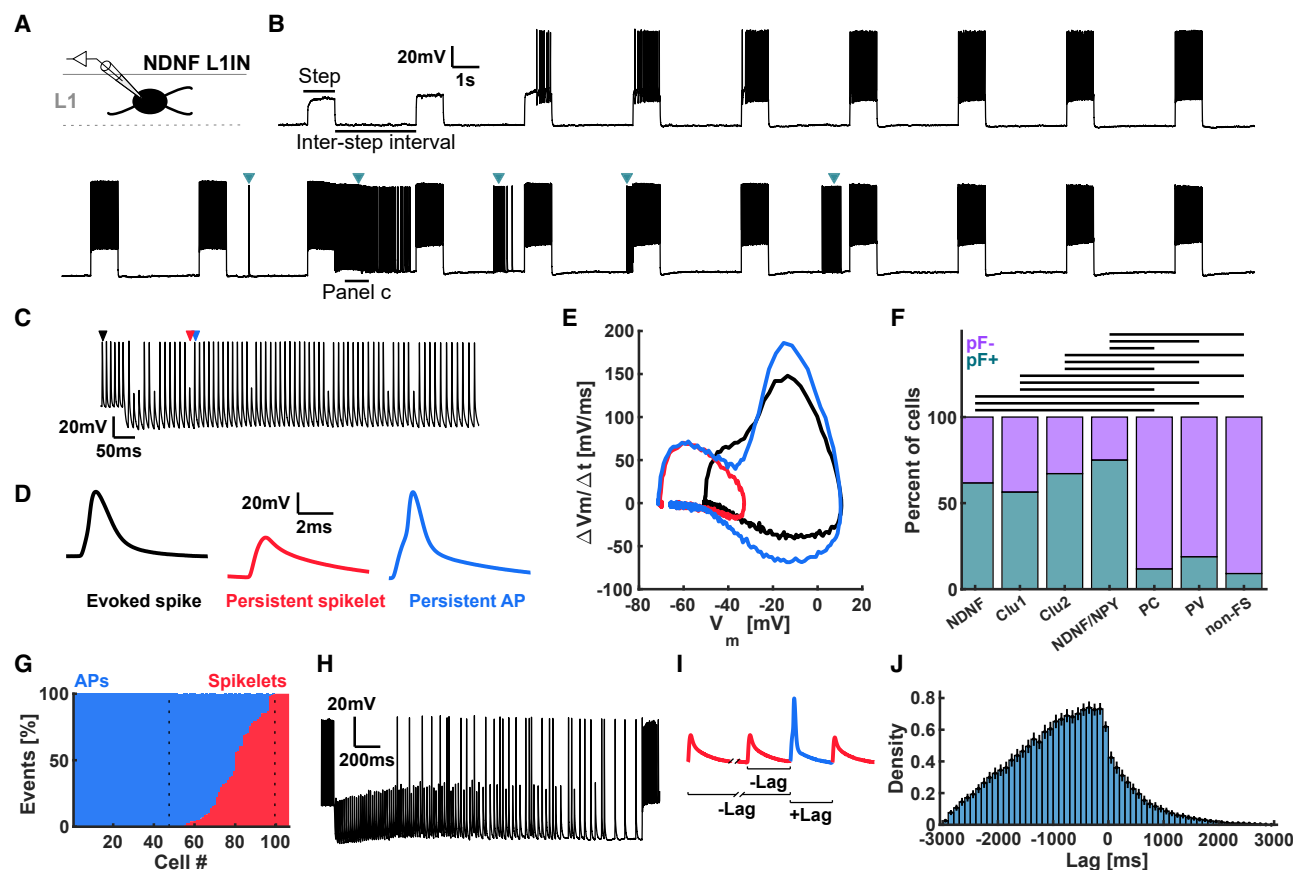


Figure 4. A specialized activity mode in NDNF L1INs

(A) Experimental design.
(B) Example recording from a genetically identified NDNF L1IN. After nine steps with current evoked spiking, the cell starts to fire spontaneously (turquoise arrows).
(C) Magnified view of the persistent firing (pF) episode in (B). Colored arrows indicate events shown in (D).
(D) Waveforms of an evoked AP (black), a persistent spikelet (red), and a persistent AP (blue).
(E) Phase plot of the events in (D). In contrast to the evoked AP (black), the persistent AP (blue) displays a deacceleration in the AP upstroke, resulting in the prominent shoulder visible in (D).
(F) Occurrence of pF by cell type ($n_{\text{NDNF}} = 128$, $n_{\text{Clu1}} = 39$, $n_{\text{Clu2}} = 70$, $n_{\text{NDNF/NPY}} = 36$, $n_{\text{PC}} = 34$, $n_{\text{PV}} = 69$, $n_{\text{nonFS}} = 44$). Eight genetically identified VIPINs were included in non-FS INs. Chi-squared test and post hoc Fisher's exact test with Bonferroni correction: $p_{\text{group}} = 3.0 \times 10^{-19}$, $p_{\text{NDNF-Clu1}} = 1$, $p_{\text{NDNF-Clu2}} = 1$, $p_{\text{NDNF-NDNF/NPY}} = 1$, $p_{\text{NDNF-PC}} = 3.1 \times 10^{-6}$, $p_{\text{NDNF-PV}} = 1.4 \times 10^{-6}$, $p_{\text{NDNF-nonFS}} = 9.8 \times 10^{-8}$, $p_{\text{Clu1-Clu2}} = 1$, $p_{\text{Clu1-NDNF/NPY}} = 1$, $p_{\text{Clu1-PC}} = 0.0016$, $p_{\text{Clu1-PV}} = 0.0021$, $p_{\text{Clu1-nonFS}} = 7.7 \times 10^{-4}$, $p_{\text{Clu2-NDNF/NPY}} = 1$, $p_{\text{Clu2-PC}} = 1.5 \times 10^{-5}$, $p_{\text{Clu2-PV}} = 1.8 \times 10^{-6}$, $p_{\text{Clu2-nonFS}} = 9.9 \times 10^{-8}$, $p_{\text{NDNF/NPY-PC}} = 1.4 \times 10^{-6}$, $p_{\text{NDNF/NPY-PV}} = 6.6 \times 10^{-7}$, $p_{\text{NDNF/NPY-nonFS}} = 2.6 \times 10^{-8}$, $p_{\text{PC-PV}} = 1$, $p_{\text{PC-nonFS}} = 1$, $p_{\text{PV-nonFS}} = 1$.
(G) Percentage of APs (blue) and spikelets (red) among persistent events by cell. Left dotted line indicates border between AP-only and AP-and-spikelet cells; right dotted line indicates border to spikelet-only cells.
(H) Example recording of an episode of pF displaying a transition from a spikelet-only phase to a spikelet-dominated and finally an AP-dominated phase.
(I) Illustration of cross-correlation analysis. For every AP, the time lag to every spikelet was measured within all episodes of pF comprising both APs and spikelets.
(J) The cross-correlation indicates that spikelets typically occur before APs during pF (179,875 pairs of 17,016 spikelets/APs in 52 cells). Data are displayed as cross-cell mean \pm SEM. See also Figures S8–S10.

of cells exhibited spikelets only (Figure 4G). Moreover, in recordings that comprised both types of events, pF typically starts with spikelets and subsequently turns into a mixture, which often ends with only APs (Figure 4H). This qualitative observation was quantitated by cross-correlating APs and spikelets per inter-step interval, which confirmed that spikelets typically preceded APs across cells (Figures 4I and 4J). In summary, we uncover pF as an attribute of NDNF L1INs that is both much less frequent and less robust in all other neuron types tested. In contrast, within

the NDNF L1IN population, pF is equally expressed irrespective of NPY co-expression or physiological cluster identity. We therefore conclude that this atypical activity mode represents a hallmark of the overall NDNF L1IN population.

Persistent firing is independent of fast synaptic transmission

We next asked whether pF is a network effect dependent on fast synaptic transmission. For this, we recorded genetically

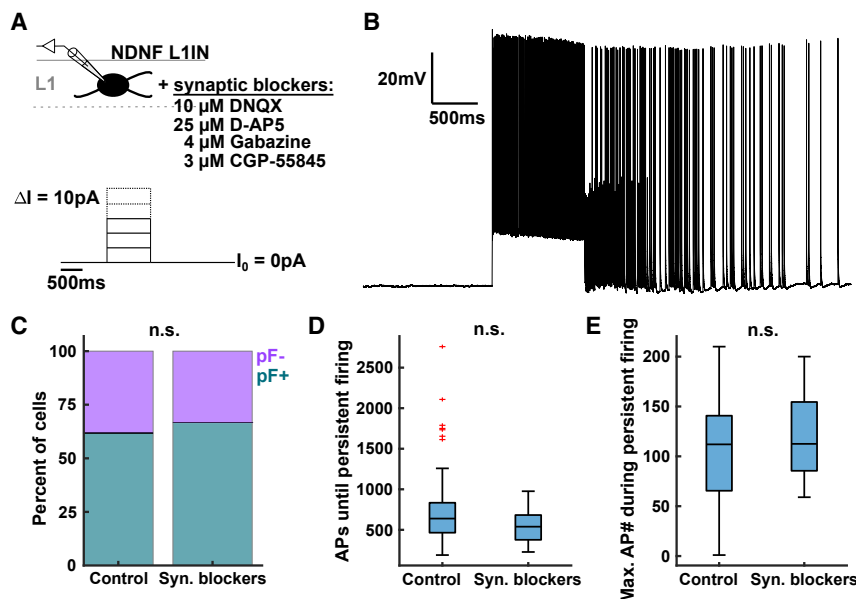


Figure 5. Persistent firing is independent of fast synaptic transmission

(A) Experimental protocol using current step injections with increasing amplitude (same as in Figure 4). In addition, blockers of fast synaptic transmission were bath applied.

(B) Example recording from an NDNF L1IN displaying persistent firing (pF) including both persistent APs and spikelets.

(C) No difference in the number of cells displaying pF was found between recordings under control conditions ($n = 128$) and in the presence of synaptic blockers ($n = 24$). Fisher's exact test $p = 0.82$.

(D and E) Among cells displaying pF, no differences to control recordings ($n = 79$) were observed in recordings in the presence of synaptic blockers ($n = 16$) in either the number of APs required to elicit pF (Wilcoxon rank-sum test $p = 0.15$, D) or in the maximum number of ectopic APs within a single inter-step interval (two-tailed t test $p = 0.26$, E). Red crosses in boxplots represent outliers and were included in the analysis.

identified NDNF L1INs employing the same protocol used to elicit pF as before. In addition, however, artificial cerebrospinal fluid (ACSF) in these experiments contained 10 μ M DNQX (6,7-dinitroquinoxaline-2,3-dione) to block AMPA (α -amino-3-hydroxy-5-methyl-4-isoxazolepropionic acid) and kainate receptors, 25 μ M D-AP5 to block N-methyl-D-aspartic acid receptors, 4 μ M SR-95531 (gabazine) to block GABA_A receptors, and 3 μ M CGP-55845 to block GABA_B receptors (Figure 5A). Despite thus blocking both glutamatergic and GABAergic signaling, we still observed pF in the majority of recorded INs (Figure 5B). Quantification yielded no differences in the occurrence of pF between recordings with vs. without synaptic blockers (control 79/128 cells or 62%, blockers 16/24 cells or 67%; Figure 5C). Furthermore, among the cells that displayed pF, we did not find any difference in the number of evoked APs required to trigger pF (median: control 639 APs, blockers 539 APs; Figure 5D) or in the maximum number of ectopic APs in a single inter-step interval (median: control 112 APs, blockers 112.5 APs; Figure 5E). We therefore conclude that, similar to previous observations in the hippocampus,³² pF in cortical NDNF L1INs is independent of fast synaptic neurotransmission.

Persistent firing is associated with a state transition in NDNF L1INs

We next asked what biological function pF of NDNF L1INs might have. The first obvious question is whether persistent activity is reflected in the synaptic output of these INs. We thus optogenetically stimulated NDNF L1INs with a protocol calibrated to evoke activity in these INs at approximately the median maximal instantaneous firing rate during pF while recording the postsynaptic response in L2/3 PCs (Figures 6A–6C, 50 Hz train). While this stimulation regime resulted in a pronounced initial outward current, the compound IPSC 80–20 decay time was 94.6 ms (Figure 6D), a value within the range of decay times of IPSCs elicited by a single LED pulse by NDNF/NPY (Figure S7D) or NDNF L1INs.¹⁶ While these experiments also revealed a sustained component, it was

extremely weak (median: 3.2 pA, approximately 10% of peak amplitude). This is consistent with the robust short-term depression of NDNF L1IN outputs even at much lower stimulation frequencies (Figures 1L and S7E) and indicates that pF can only transiently cause substantial levels of inhibition. Given that the average duration of episodes of pF by far exceeded the time window of postsynaptic transfer, we wondered whether pF might have additional, perhaps cell-autonomous effects in NDNF L1INs themselves. Indeed, we noted that the onset of pF was associated with a sudden depolarization as well as the emergence of an after-step hyperpolarization (ASH) at the offset of the depolarizing current steps (Figures S11A–S11C). In addition, we observed that NDNF L1INs that display pF reach higher evoked firing rates than those that do not (Figure S11D). Since the recording protocol with escalating current steps makes it difficult to disambiguate the effects of pF from those of stronger exogenous stimulation, we switched to a series of current steps with constant amplitude calibrated to evoke APs at approximately 28 Hz in the first step, a frequency that provides enough dynamic range to detect changes in firing rate in either direction (Figures 6E, 6F, and S11E). Consistent with our previous results, when applying the same criterion for pF as above, a large fraction of recorded NDNF L1INs displayed pF (18/28 or 64%, Figures 6F–6H, S11E, and S11F). Intriguingly, in the cells displaying persistent firing, we observed that evoked firing rates started to increase a few steps before, and peaked shortly before, onset of pF (Figures 6I, 6J, and S11G). Evoked firing rates decreased again after onset of pF but remained constantly elevated relative to initial firing rates over tens of seconds until the end of the recording (Figures 6I, 6J, and S11G). In contrast, these dynamics were completely absent in NDNF L1INs without pF. In fact, except for an initial, much smaller increase after the first step, firing rates were practically constant. Strikingly, we observed similar dynamics for the threshold of evoked APs, which started to decrease toward onset of pF, with a minimum immediately before the onset (Figures 6K, 6L, and S11H). Similar to evoked firing rates, AP thresholds started to increase again after onset of pF but did not

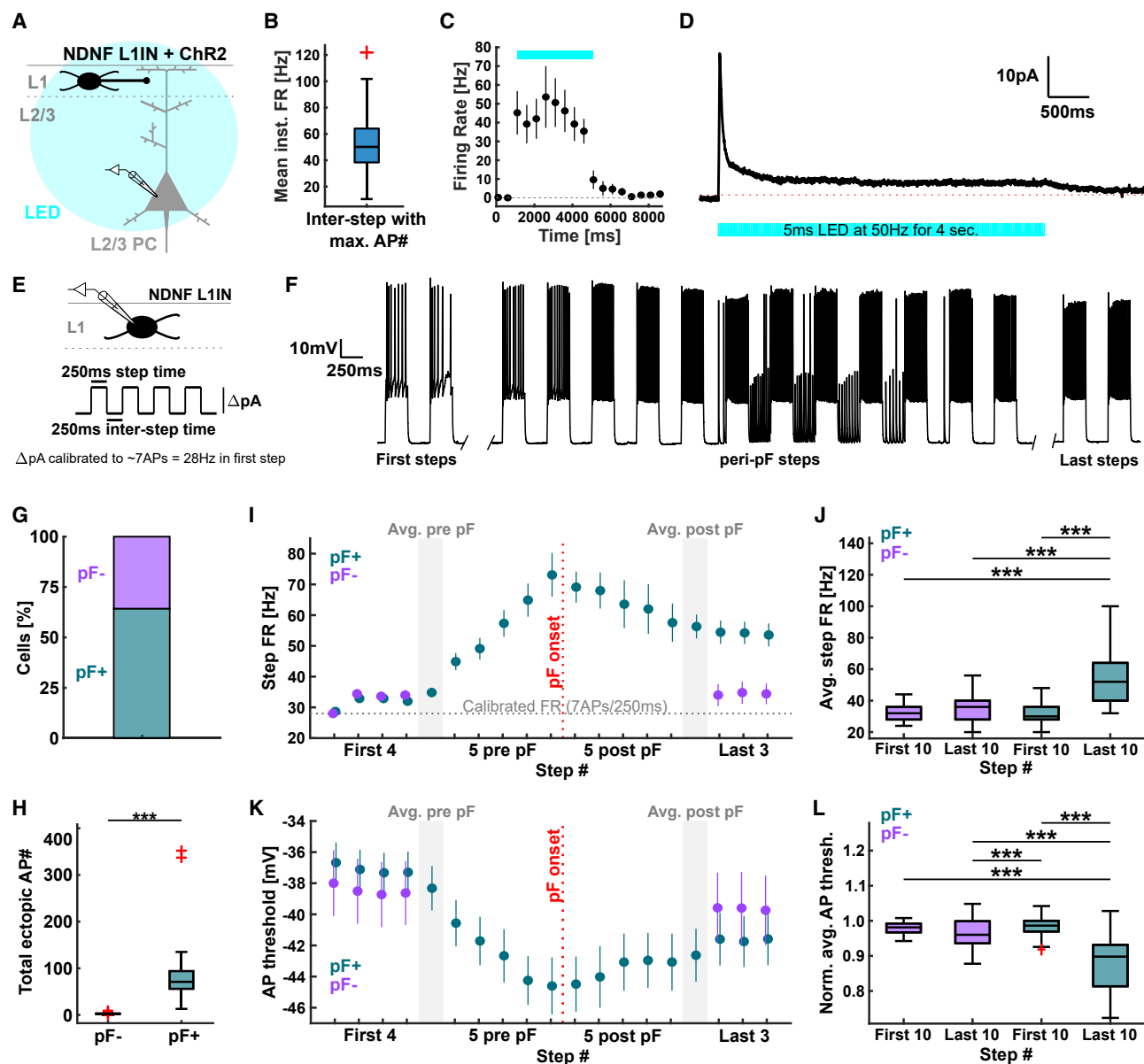


Figure 6. Persistent firing is associated with a state transition in NDNF L1INs

(A) Experimental design to test postsynaptic effects of simulated persistent firing (pF) in NDNF L1INs by optogenetic stimulation at 50 Hz for 4 s.

(B) Mean instantaneous pF rate in the inter-step interval with the maximum number of ectopic action potentials ($n = 79$ cells). Mean = 51.2 Hz, median = 50.1 Hz.

(C) Optogenetic activation was calibrated to achieve a sustained firing rate of approximately 50 Hz in the population average (5-ms pulses, $n = 10$ cells).

(D) Grand average trace of IPSCs in L2/3 PCs ($n = 12$). Red line indicates pre-IPSC baseline.

(E) Experimental design. NDNF L1INs were stimulated with constant amplitude current steps of 250 ms duration at 2 Hz. Amplitudes were calibrated for each cell to elicit APs at approximately 28 Hz in the first step.

(F) Example recording of an NDNF L1IN displaying pF. Left: first two steps. Center: steps immediately preceding/following pF. Right: Last two steps in recording.

(G) Percentage of NDNF L1INs ($n = 28$) displaying pF during the protocol.

(H) Total number of ectopic APs in cells that do ($n = 18$) or do not ($n = 10$) display pF. Wilcoxon rank-sum test $p = 1.74e-5$.

(I) Evoked firing rates over time ($n_{pF+} = 18$, $n_{pF-} = 10$). Data displayed as mean \pm SEM. Red line indicates pF onset.

(J) Comparison of firing rates in first 10 vs. last 10 steps by presence or absence of pF ($n_{pF+} = 18$, $n_{pF-} = 10$). Kruskal-Wallis test $p_{\text{group}} = 6.8e-61$. Post hoc Dunn's test $p_{\text{first--last-}} = 1$, $p_{\text{first--first+}} = 0.45$, $p_{\text{first--last+}} = 0$, $p_{\text{last--first+}} = 0.18$, $p_{\text{last--last+}} = 0$, $p_{\text{first+--last+}} = 0$.

(K) Same as (I) for the threshold of evoked APs ($n_{pF+} = 18$, $n_{pF-} = 10$).

(legend continued on next page)

return to initial values until the end of the recording. Again, NDNF L1INs without pF showed no such dynamics. Notably, this state of enhanced excitability was long-lasting and, in particular, the increased firing rates could be sustained for as long as the cell was continuously stimulated (up to several minutes). In contrast, a prolonged resting period without any stimulation (at least ~30 s) resulted in a return to the initial electrophysiological state. This cycle of stimulation, pF, and transition to a highly excitable state, and return to the initial state after a period of rest, could be repeated many times in the same cell. Together, these data indicate that whereas pF only causes transient postsynaptic inhibition, it is associated with a profound and long-lasting transition in the intrinsic state of NDNF L1INs toward greater excitability.

DISCUSSION

NDNF L1INs have recently emerged as a type of IN in mouse and human neocortex that is distinct from the much more intensely investigated populations expressing PV, SST, and VIP.^{16–21} Despite the fact that NDNF L1INs display a range of specialized and intriguing attributes, including robust encoding of experience¹⁶ and arousal,¹⁸ rapid neuromodulation,²¹ and input from a large number of brain-wide afferents conveying top-down information,^{1,8,16–20} our understanding of the intrinsic and circuit function of these neurons has remained incomplete. Here, we use *in vitro* patch-clamp recordings combined with single and intersectional genetic targeting, *in situ* hybridization, unbiased clustering, and optogenetics to close this gap in our understanding.

Integration into the neocortical circuit

Our data reveal that NDNF L1INs not only inhibit the distal apical dendrites of PCs in L1^{16,17} but at the same time pervasively inhibit the majority of L2/3INs, including those expressing VIP and PV. As NDNF L1INs themselves receive strong and diverse long-range top-down projections,^{7,8,16–18,20} these findings therefore define NDNF L1INs as top-down master regulators of the superficial cortex.⁹ Intriguingly, the one IN type that is not substantially inhibited by NDNF L1INs are SSTINs^{16–18} (median IPSC amplitude across all recordings 1.9 pA, Figure 1G), whereas the connection from SSTINs to NDNF L1INs is more than two orders of magnitude stronger.¹⁶ Like NDNF L1INs, SSTINs have been described as cortical master regulators⁹ based on the fact that they, too, broadly inhibit cortical INs^{9,26} as well as PC apical dendrites.^{23,25} However, SSTINs are most strongly driven by local recurrent activity^{22–24} and, moreover, strongly inhibit NDNF L1INs.¹⁶ In summary, this similarity in output connectivity together with the contrast in *in vivo* encoding,^{16–20,22–24} potentially opposing roles during learning,^{16,19} the largely unidirectional inhibition between the two cell types,^{9,16–18} and the fact that the pronounced short-term depression of NDNF L1IN outputs will favor low frequency signaling, whereas the opposite has been proposed for

SSTINs,^{23–25} define the working hypothesis of two hierarchically organized cortical master regulators recruited by local recurrent vs. long-range top-down information. Future experimental and theoretical work addressing how these IN types interact *in vivo* during integration of bottom-up and top-down information is therefore required.^{16,19,50}

Similarly, connectivity between NDNF L1INs and superficial VIPINs is unidirectional as well: while we find that NDNF L1INs inhibit superficial VIPINs, the reverse is not the case.¹⁶ Both IN types are targeted by top-down afferents^{16–18,24,51} and key elements in local disinhibitory circuits.^{17,18,24,27,51} However, whereas NDNF L1INs directly inhibit PC dendrites and indirectly—via PVINs—disinhibit PC somata, VIPINs indirectly—via SSTINs—disinhibit PC dendrites and—via disinhibition of PVINs—enhance inhibition of PC somata.^{16–18,23,24,26,51} The two IN types therefore produce opposing effects on PCs, and the unidirectional connectivity we uncover suggests a functional hierarchy between the two disinhibitory circuits.

Potential subtypes of NDNF L1INs

Given the pervasive finding that IN types identified by single genetic markers can be further subdivided into distinct subclasses,²⁷ we utilized intersectional genetic targeting to address this issue for NDNF L1INs. While the overall population of NDNF cells falls apart into two physiological clusters, we found no correspondence of these attributes with co-expression of NPY. Moreover, NPY⁺ and NPY[−] NDNF L1INs display similar incidence of pF, IPSC kinetics, and circuit connectivity, together indicating that there is insufficient functional distinction for dubbing NPY⁺ NDNF L1INs a distinct subclass of IN. In contrast, previous work in juvenile somatosensory cortex (age post-natal day 21 [P21]–P53)²⁸ reported a clear separation between NPY⁺ and NPY[−] NDNF L1INs, while a continuum of attributes between NPY⁺ and NPY[−] L1INs expressing Lamp5-MET1 (a population largely overlapping with NDNF in L1⁴⁸) was found in visual cortex of young adults (age P45–P70).⁴⁸ While these apparent discrepancies may thus also be due to area differences, a perhaps more likely explanation relates to the fact that, different from most canonical IN markers, expression of NPY in INs expands continuously with age.⁵² Consistent with this, our *in situ* hybridization experiments indicate that ~65% of *Ndnf* INs co-express *Npy* in mature adults (295/447, Figure S4F), whereas this number drops to ~40% in juvenile mice.²⁸ We therefore submit that NPY may be a good marker to define NDNF L1IN subpopulations in juvenile neocortex but becomes less specific with age.

Persistent firing, a specialized activity mode of NDNF L1INs

Whereas the overwhelming number of neuron types exclusively functions as signal integrators, our data uncover that after sufficient stimulation, the majority of NDNF L1INs switches to becoming signal generators by persistently producing APs in the absence of stimulation. Persistent firing originates in the

Data displayed as mean ± SEM. Red line indicates onset of pF.

(L) Same as (J) for the threshold of evoked APs. Kruskal-Wallis test $p_{\text{group}} = 7.4\text{e}^{-48}$. Post hoc Dunn's test $p_{\text{first} \rightarrow \text{last}} = 0.065$, $p_{\text{first} \rightarrow \text{first}+} = 0.87$, $p_{\text{first} \rightarrow \text{last}+} = 0$, $p_{\text{last} \rightarrow \text{first}+} = 4.7\text{e}^{-6}$, $p_{\text{last} \rightarrow \text{last}+} = 0$, $p_{\text{first}+ \rightarrow \text{last}+} = 0$.

Red crosses in boxplots represent outliers and were included in the analysis. See also Figure S11.

distal axon^{31,32} and has primarily been observed in hippocampal and cortical NGFCs.^{30–33,53} In line with this, we find that while pF occurs in a large proportion of NDNF L1INs, we observe it only rarely and much more weakly in other cortical cell types.

Functionally, our results indicate that pF does not elicit robust and sustained postsynaptic inhibition due to the robust short-term depression we observe. In contrast, we find that pF is associated with a profound and long-lasting transition in NDNF L1IN electrophysiological state, including changes in resting membrane potential, ASH, and AP threshold and firing rate. Our data therefore argue for a cell-autonomous effect of pF that may, for instance, modulate the induction of long-term synaptic plasticity at the afferents of these cells.^{30,54} In the temporal domain, the long-lasting nature of pF is in line with several other NDNF L1IN characteristics that occur on protracted timescales, including late-spiking slow single IPSC kinetics, pronounced short-term depression, and the fact that top-down inputs often display much greater latencies than bottom-up signals.¹ Together, this argues for NDNF L1INs as a neuron type that is optimized for slow signals.

Limitations of the study

While our approach for determining the output connectivity of NDNF L1INs by optogenetic activation at the population level yields robust results, it cannot resolve the organization of individual NDNF L1IN outputs. It therefore remains to be determined whether single NDNF L1INs indiscriminately target PCs and interneurons or whether there is a selectivity based, e.g., on target cell type or distance, as has recently been demonstrated for inhibition of PCs by NDNF L1INs.^{17,28}

Likewise, we focus here on postsynaptic targets of NDNF L1INs in L2/3. Together with previous work demonstrating that NDNF L1INs target both NDNF and non-NDNF INs in L1^{16,28} as well as L5 pyramidal neurons,^{16,17} this reveals NDNF L1INs as cortical master regulators. However, whether and how NDNF L1INs also connect to different IN types in L4–L6 remains an open question that should be addressed in future work.

Finally, it needs to be determined how our *in vitro* findings on pF and the associated excitability changes map onto the situation in the intact animal. While it has been demonstrated that pF can occur *in vivo*,³¹ future experiments are required to elucidate the precise conditions under which this activity mode is induced in the intact animal. Since L1INs can be robustly activated by acetylcholine release,^{21,39} one promising and testable hypothesis is that pF and the associated excitability changes may be recruited during brain states with strong cholinergic tone, such as attention, learning, and locomotion.⁵⁵

STAR★METHODS

Detailed methods are provided in the online version of this paper and include the following:

- KEY RESOURCES TABLE
- RESOURCE AVAILABILITY
 - Lead contact
 - Materials availability
 - Data and code availability
- METHOD DETAILS

- Animal subjects
- Surgery
- Slice preparation
- Patch clamp electrophysiology
- Fluorescent *in situ* hybridization (FISH)

● QUANTIFICATION AND STATISTICAL ANALYSIS

SUPPLEMENTAL INFORMATION

Supplemental information can be found online at <https://doi.org/10.1016/j.celrep.2024.114212>.

ACKNOWLEDGMENTS

We thank all members of the Letzkus lab, M. Bartos, and H. Sprekeler for discussions; A. Wrana and U. Thirumanna for technical assistance; and K. Deisseroth and E.S. Boyden for generously sharing reagents. This work was supported by the German Research Foundation LE 3804/3-1, German Research Foundation LE 3804/4-1, German Research Foundation LE 3804/7-1, German Research Foundation LE 3804/8-1, and German Research Foundation TRR 384/1 2024, 514483642 to J.J.L.; the BrainLinks-BrainTools – IMBIT center to J.H.; and the Peter and Traudl Engelhorn Foundation Postdoctoral Fellowship and Brain and Behavior Research Foundation (31041) to A.S.

AUTHOR CONTRIBUTIONS

Conceptualization, J.H. and J.J.L.; methodology, A.S. and R.B.P.; investigation, J.H. (Figures 1, 2, 3, 4, 5, and 6), A.S. (Figure 3), and R.A.P.V. (Figures 3 and 4); analysis, J.H.; visualization, J.H.; supervision, J.J.L.; writing, J.H. and J.J.L.

DECLARATION OF INTERESTS

The authors declare no competing interests.

Received: January 10, 2024

Revised: March 10, 2024

Accepted: April 23, 2024

Published: May 13, 2024

REFERENCES

1. Pardi, M.B., Schroeder, A., and Letzkus, J.J. (2023). Probing top-down information in neocortical layer 1. *Trends Neurosci.* 46, 20–31. <https://doi.org/10.1016/j.tins.2022.11.001>.
2. Schuman, B., Dellal, S., Prönneke, A., Machold, R., and Rudy, B. (2021). Neocortical Layer 1: An Elegant Solution to Top-Down and Bottom-Up Integration. *Annu. Rev. Neurosci.* 44, 221–252. <https://doi.org/10.1146/annurev-neuro-100520-012117>.
3. Shin, J.N., Doron, G., and Larkum, M.E. (2021). Memories off the top of your head. *Science* 374, 538–539. <https://doi.org/10.1126/science.abk1859>.
4. Mitchell, B.D., and Cauler, L.J. (2001). Corticocortical and thalamocortical projections to layer I of the frontal neocortex in rats. *Brain Res.* 921, 68–77. [https://doi.org/10.1016/S0006-8993\(01\)03084-0](https://doi.org/10.1016/S0006-8993(01)03084-0).
5. Doron, G., Shin, J.N., Takahashi, N., Drücke, M., Bocklisch, C., Skenderi, S., de Mont, L., Toumazou, M., Ledderose, J., Brecht, M., et al. (2020). Perirhinal input to neocortical layer 1 controls learning. *Science* 370, eaaz3136. <https://doi.org/10.1126/science.aaz3136>.
6. Keller, G.B., and Mrisic-Flogel, T.D. (2018). Predictive Processing: A Canonical Cortical Computation. *Neuron* 100, 424–435. <https://doi.org/10.1016/j.neuron.2018.10.003>.
7. Pardi, M.B., Vogenstahl, J., Dalmay, T., Spanò, T., Pu, D.-L., Naumann, L.B., Kretschmer, F., Sprekeler, H., and Letzkus, J.J. (2020). A

- thalamocortical top-down circuit for associative memory. *Science* 370, 844–848. <https://doi.org/10.1126/science.abc2399>.
8. Schroeder, A., Pardi, M.B., Keijsers, J., Dalmay, T., Groisman, A.I., Schuman, E.M., Sprekeler, H., and Letzkus, J.J. (2023). Inhibitory top-down projections from zona incerta mediate neocortical memory. *Neuron* 111, 727–738.e8. <https://doi.org/10.1016/j.neuron.2022.12.010>.
9. Jiang, X., Shen, S., Cadwell, C.R., Berens, P., Sinz, F., Ecker, A.S., Patel, S., and Tolias, A.S. (2015). Principles of connectivity among morphologically defined cell types in adult neocortex. *Science* 350, aac9462. <https://doi.org/10.1126/science.aac9462>.
10. Egger, R., Schmitt, A.C., Wallace, D.J., Sakmann, B., Oberlaender, M., and Kerr, J.N.D. (2015). Robustness of sensory-evoked excitation is increased by inhibitory inputs to distal apical tuft dendrites. *Proc. Natl. Acad. Sci. USA* 112, 14072–14077. <https://doi.org/10.1073/pnas.1518773112>.
11. Jiang, X., Wang, G., Lee, A.J., Stornetta, R.L., and Zhu, J.J. (2013). The organization of two new cortical interneuronal circuits. *Nat. Neurosci.* 16, 210–218. <https://doi.org/10.1038/nn.3305>.
12. Muralidhar, S., Wang, Y., and Markram, H. (2013). Synaptic and cellular organization of layer 1 of the developing rat somatosensory cortex. *Front. Neuroanat.* 7, 52.
13. Fishell, G., and Kepecs, A. (2020). Interneuron Types as Attractors and Controllers. *Annu. Rev. Neurosci.* 43, 1–30. <https://doi.org/10.1146/annurev-neuro-070918-050421>.
14. Lourenço, J., Koukoulis, F., and Bacci, A. (2020). Synaptic inhibition in the neocortex: Orchestration and computation through canonical circuits and variations on the theme. *Cortex* 132, 258–280. <https://doi.org/10.1016/j.cortex.2020.08.015>.
15. Wester, J.C., and McBain, C.J. (2014). Behavioral state-dependent modulation of distinct interneuron subtypes and consequences for circuit function. *Curr. Opin. Neurobiol.* 29, 118–125. <https://doi.org/10.1016/j.conb.2014.07.007>.
16. Abs, E., Poorthuis, R.B., Apelblat, D., Muhammad, K., Pardi, M.B., Enke, L., Kushinsky, D., Pu, D.-L., Eizinger, M.F., Conzelmann, K.-K., et al. (2018). Learning-Related Plasticity in Dendrite-Targeting Layer 1 Interneurons. *Neuron* 100, 684–699.e6. <https://doi.org/10.1016/j.neuron.2018.09.001>.
17. Anastasiades, P.G., Collins, D.P., and Carter, A.G. (2021). Mediodorsal and Ventromedial Thalamus Engage Distinct L1 Circuits in the Prefrontal Cortex. *Neuron* 109, 314–330.e4. <https://doi.org/10.1016/j.neuron.2020.10.031>.
18. Cohen-Kashi Malina, K., Tsivourakis, E., Kushinsky, D., Apelblat, D., Shtiglitz, S., Zohar, E., Sokoletsky, M., Tasaka, G.I., Mizrahi, A., Lampl, I., and Spiegel, I. (2021). NDNF interneurons in layer 1 gain-modulate whole cortical columns according to an animal's behavioral state. *Neuron* 109, 2150–2164.e5. <https://doi.org/10.1016/j.neuron.2021.05.001>.
19. Hartung, J., and Letzkus, J.J. (2021). Inhibitory plasticity in layer 1 – dynamic gatekeeper of neocortical associations. *Curr. Opin. Neurobiol.* 67, 26–33. <https://doi.org/10.1016/j.conb.2020.06.003>.
20. Ibrahim, L.A., Huang, S., Fernandez-Otero, M., Sherer, M., Qiu, Y., Vemuri, S., Xu, Q., Machold, R., Pouchelon, G., Rudy, B., and Fishell, G. (2021). Bottom-up inputs are required for establishment of top-down connectivity onto cortical layer 1 neurogliaform cells. *Neuron* 109, 3473–3485.e5. <https://doi.org/10.1016/j.neuron.2021.08.004>.
21. Poorthuis, R.B., Muhammad, K., Wang, M., Verhoog, M.B., Junek, S., Wrana, A., Mansvelder, H.D., and Letzkus, J.J. (2018). Rapid Neuromodulation of Layer 1 Interneurons in Human Neocortex. *Cell Rep.* 23, 951–958. <https://doi.org/10.1016/j.celrep.2018.03.111>.
22. Adesnik, H., Bruns, W., Taniguchi, H., Huang, Z.J., and Scanziani, M. (2012). A neural circuit for spatial summation in visual cortex. *Nature* 490, 226–231. <https://doi.org/10.1038/nature11526>.
23. Urban-Ciecko, J., and Barth, A.L. (2016). Somatostatin-expressing neurons in cortical networks. *Nat. Rev. Neurosci.* 17, 401–409. <https://doi.org/10.1038/nrn.2016.53>.
24. Yavorska, I., and Wehr, M. (2016). Somatostatin-Expressing Inhibitory Interneurons in Cortical Circuits. *Front. Neural Circ.* 10, 76.
25. Wu, S.J., Sevier, E., Dwivedi, D., Saldi, G.-A., Hairston, A., Yu, S., Abbott, L., Choi, D.H., Sherer, M., Qiu, Y., et al. (2023). Cortical somatostatin interneuron subtypes form cell-type-specific circuits. *Neuron* 111, 2675–2692.e9. <https://doi.org/10.1016/j.neuron.2023.05.032>.
26. Pfeffer, C.K., Xue, M., He, M., Huang, Z.J., and Scanziani, M. (2013). Inhibition of inhibition in visual cortex: the logic of connections between molecularly distinct interneurons. *Nat. Neurosci.* 16, 1068–1076. <https://doi.org/10.1038/nn.3446>.
27. Luo, L., Callaway, E.M., and Svoboda, K. (2018). Genetic Dissection of Neural Circuits: A Decade of Progress. *Neuron* 98, 256–281. <https://doi.org/10.1016/j.neuron.2018.03.040>.
28. Schuman, B., Machold, R.P., Hashikawa, Y., Fuzik, J., Fishell, G.J., and Rudy, B. (2019). Four Unique Interneuron Populations Reside in Neocortical Layer 1. *J. Neurosci.* 39, 125–139. <https://doi.org/10.1523/JNEUROSCI.1613-18.2018>.
29. Fenno, L.E., Mattis, J., Ramakrishnan, C., Hyun, M., Lee, S.Y., He, M., Tucciarone, J., Selimbeyoglu, A., Berndt, A., Grosenick, L., et al. (2014). Targeting cells with single vectors using multiple-feature Boolean logic. *Nat. Methods* 11, 763–772. <https://doi.org/10.1038/nmeth.2996>.
30. Chittajallu, R., Auvill, K., Mahadevan, V., Lai, M., Hunt, S., Calvigioni, D., Pelkey, K.A., Zaghloul, K.A., and McBain, C.J. (2020). Activity-dependent tuning of intrinsic excitability in mouse and human neurogliaform cells. *Elife* 9, e57571. <https://doi.org/10.7554/eLife.57571>.
31. Rózsa, M., Tóth, M., Oláh, G., Baka, J., Lákócs, R., Barzó, P., and Tamás, G. (2023). Temporal disparity of action potentials triggered in axon initial segments and distal axons in the neocortex. *Sci. Adv.* 9, eade4511. <https://doi.org/10.1126/sciadv.ade4511>.
32. Sheffield, M.E.J., Best, T.K., Mensh, B.D., Kath, W.L., and Spruston, N. (2011). Slow integration leads to persistent action potential firing in distal axons of coupled interneurons. *Nat. Neurosci.* 14, 200–207. <https://doi.org/10.1038/nn.2728>.
33. Sheffield, M.E.J., Edgerton, G.B., Heuermann, R.J., Deemyad, T., Mensh, B.D., and Spruston, N. (2013). Mechanisms of retroaxonal barrage firing in hippocampal interneurons. *J. Physiol.* 591, 4793–4805. <https://doi.org/10.1113/jphysiol.2013.258418>.
34. Elgueta, C., Köhler, J., and Bartos, M. (2015). Persistent Discharges in Dentate Gyrus Perisoma-Inhibiting Interneurons Require Hyperpolarization-Activated Cyclic Nucleotide-Gated Channel Activation. *J. Neurosci.* 35, 4131–4139. <https://doi.org/10.1523/JNEUROSCI.3671-14.2015>.
35. Froemke, R.C. (2015). Plasticity of Cortical Excitatory-Inhibitory Balance. *Annu. Rev. Neurosci.* 38, 195–219. <https://doi.org/10.1146/annurev-neuro-071714-034002>.
36. Kepecs, A., and Fishell, G. (2014). Interneuron cell types are fit to function. *Nature* 505, 318–326. <https://doi.org/10.1038/nature12983>.
37. Letzkus, J.J., Wolff, S.B.E., and Lüthi, A. (2015). Disinhibition, a Circuit Mechanism for Associative Learning and Memory. *Neuron* 88, 264–276. <https://doi.org/10.1016/j.neuron.2015.09.024>.
38. Loomba, S., Straehle, J., Gangadharan, V., Heike, N., Khalifa, A., Motta, A., Ju, N., Sievers, M., Gempt, J., Meyer, H.S., and Helmstaedter, M. (2022). Connectomic comparison of mouse and human cortex. *Science* 377, eabo0924. <https://doi.org/10.1126/science.abo0924>.
39. Letzkus, J.J., Wolff, S.B.E., Meyer, E.M.M., Tovote, P., Courtin, J., Herry, C., and Lüthi, A. (2011). A disinhibitory microcircuit for associative fear learning in the auditory cortex. *Nature* 480, 331–335. <https://doi.org/10.1038/nature10674>.
40. Taniguchi, H., He, M., Wu, P., Kim, S., Paik, R., Sugino, K., Kvitsiani, D., Fu, Y., Lu, J., Lin, Y., et al. (2011). A Resource of Cre Driver Lines for Genetic

- Targeting of GABAergic Neurons in Cerebral Cortex. *Neuron* 71, 995–1013. <https://doi.org/10.1016/j.neuron.2011.07.026>.
41. Vormstein-Schneider, D., Lin, J.D., Pelkey, K.A., Chittajallu, R., Guo, B., Arias-Garcia, M.A., Allaway, K., Sakopoulos, S., Schneider, G., Stevenson, O., et al. (2020). Viral manipulation of functionally distinct interneurons in mice, non-human primates and humans. *Nat. Neurosci.* 23, 1629–1636. <https://doi.org/10.1038/s41593-020-0692-9>.
42. Chan, K.Y., Jang, M.J., Yoo, B.B., Greenbaum, A., Ravi, N., Wu, W.-L., Sánchez-Guardado, L., Lois, C., Mazmanian, S.K., Deverman, B.E., and Gradinaru, V. (2017). Engineered AAVs for efficient noninvasive gene delivery to the central and peripheral nervous systems. *Nat. Neurosci.* 20, 1172–1179. <https://doi.org/10.1038/nn.4593>.
43. Hu, H., Gan, J., and Jonas, P. (2014). Fast-spiking, parvalbumin + GABAergic interneurons: From cellular design to microcircuit function. *Science* 345, 1255263. <https://doi.org/10.1126/science.1255263>.
44. Hestrin, S., and Armstrong, W.E. (1996). Morphology and Physiology of Cortical Neurons in Layer I. *J. Neurosci.* 16, 5290–5300. <https://doi.org/10.1523/JNEUROSCI.16-17-05290.1996>.
45. Boldog, E., Bakken, T.E., Hodge, R.D., Novotny, M., Aebermann, B.D., Baka, J., Bordé, S., Close, J.L., Díez-Fuertes, F., Ding, S.-L., et al. (2018). Transcriptomic and morphophysiological evidence for a specialized human cortical GABAergic cell type. *Nat. Neurosci.* 21, 1185–1195. <https://doi.org/10.1038/s41593-018-0205-2>.
46. Chartrand, T., Dalley, R., Close, J., Goriounova, N.A., Lee, B.R., Mann, R., Miller, J.A., Molnar, G., Mukora, A., Alfiler, L., et al. (2023). Morphoelectric and transcriptomic divergence of the layer 1 interneuron repertoire in human versus mouse neocortex. *Science* 382, eadf0805. <https://doi.org/10.1126/science.adf0805>.
47. Overstreet-Wadiche, L., and McBain, C.J. (2015). Neurogliaform cells in cortical circuits. *Nat. Rev. Neurosci.* 16, 458–468. <https://doi.org/10.1038/nrn3969>.
48. Gouwens, N.W., Sorensen, S.A., Baftizadeh, F., Budzillo, A., Lee, B.R., Jarsky, T., Alfiler, L., Baker, K., Barkan, E., Berry, K., et al. (2020). Integrated Morphoelectric and Transcriptomic Classification of Cortical GABAergic Cells. *Cell* 183, 935–953.e19. <https://doi.org/10.1016/j.cell.2020.09.057>.
49. Schulz, J.M., Kay, J.W., Bischofberger, J., and Larkum, M.E. (2021). GABAB Receptor-Mediated Regulation of Dendro-Somatic Synergy in Layer 5 Pyramidal Neurons. *Front. Cell. Neurosci.* 15, 718413. <https://doi.org/10.3389/fncel.2021.718413>.
50. Naumann, L., Hertäg, L., and Sprekeler, H. (2023). Layer-specific control of cortical inhibition by NDNF interneurons. In *Science Communications World Wide*. <https://doi.org/10.57736/97DF-B456>.
51. Apicella, A.J., and Marchionni, I. (2022). VIP-Expressing GABAergic Neurons: Disinhibitory vs. Inhibitory Motif and Its Role in Communication Across Neocortical Areas. *Front. Cell. Neurosci.* 16, 811484. <https://doi.org/10.3389/fncel.2022.811484>.
52. Ouellet, L., and de Villers-Sidani, E. (2014). Trajectory of the main GABAergic interneuron populations from early development to old age in the rat primary auditory cortex. *Front. Neuroanat.* 8. <https://doi.org/10.3389/fnana.2014.00040>.
53. Deemyad, T., Lüthi, J., and Spruston, N. (2018). Astrocytes integrate and drive action potential firing in inhibitory subnetworks. *Nat. Commun.* 9, 4336. <https://doi.org/10.1038/s41467-018-06338-3>.
54. Mercier, M.S., Magloire, V., Cornford, J.H., and Kullmann, D.M. (2022). Long-term potentiation in neurogliaform interneurons modulates excitation–inhibition balance in the temporoammonic pathway. *J. Physiol.* 600, 4001–4017. <https://doi.org/10.1113/JP282753>.
55. Poorthuis, R.B., Enke, L., and Letzkus, J.J. (2014). Cholinergic circuit modulation through differential recruitment of neocortical interneuron types during behaviour. *J. Physiol.* 592, 4155–4164. <https://doi.org/10.1113/jphysiol.2014.273862>.

STAR★METHODS

KEY RESOURCES TABLE

REAGENT or RESOURCE	SOURCE	IDENTIFIER
Antibodies		
Chicken polyclonal anti-GFP	Aves Labs	Cat# GFP-1020; RRID: AB_10000240
Goat anti-chicken, Alexa 488	Thermo Fisher Scientific	Cat# A-11039; RRID: AB_253409
Bacterial and virus strains		
AAV2/1.CAG.Flex.tdTomato.WPRE.bGH	PennVector Core	Cat# AV-1-ALL864
AAV2/5.EF1a.DIO.hChR2(H134R)-EYFP.WPRE.hGH	PennVector Core	Cat# AV-5-20298P
AAV2/1-EF1a-fDIO-ChrimsonR-wpre-sv40	Vector Biolabs	N/A
AAV2/1-EF1a-fDIO-EYFP-WPRE	UNC Vector Core	Cat# AV6154B
AAV2/5-hSyn-Con/Fon EYFP-WPRE	UNC Vector Core	Cat# AV8357
AAV2/5-hSyn-Con/Fon hChR2(H134R)-EYFP-WPRE	UNC Vector Core	Cat# AV8358
pAAV-mDLX-NLS-mRuby (AAV9)	Chan et al. ⁴²	addgene, Cat# 99130-AAV9
pAAV-S5E2-Gq-P2A-dTomato (AAV9)	Vormstein-Schneider et al. ⁴¹	addgene, Cat# 135634-AAV9
Chemicals, peptides, and recombinant proteins		
RNAscope Probe Diluent	Advanced Cell Diagnostics	Cat# 300041
RNAscope Probe Mm-Npy-C2	Advanced Cell Diagnostics	Cat# 313321-C2
RNAscope Probe Mm-Ndnf-C3	Advanced Cell Diagnostics	Cat# 447471-C3
CGP-55845	Sigma	Cat# SML0594
Critical commercial assays		
RNAscope Fluorescent Multiplex Kit	Advanced Cell Diagnostics	Cat# 320850
Deposited data		
Figures 1, 2, and 4–6 and electrophysiological data from Figure 3	This paper	https://doi.org/10.5281/zenodo.10938947
Histological data from Figure 3 (part 1)	This paper	https://doi.org/10.5281/zenodo.10938467
Histological data from Figure 3 (part 2)	This paper	https://doi.org/10.5281/zenodo.10938471
Experimental models: Organisms/strains		
B6(Cg)-Ndnf ^{tm1.1(cre/ERT2)spgl/J}	Ivo Spiegel (available at The Jackson Laboratory)	Cat# 034875; RRID: IMSR_JAX:034875
B6(Cg)-Ndnf ^{tm1.1(fipo)spgl/J}	Johannes Letzkus and Ivo Spiegel (available at The Jackson Laboratory)	Cat# 034876; RRID: IMSR_JAX:034876
B6.Cg-Gt(ROSA)26Sor ^{tm9(CAG-tdTomato)Hze/J}	The Jackson Laboratory	Cat# 007909; RRID: IMSR_JAX:007909
STOCK <i>Vip</i> ^{tm1(cre)Zjh/J}	The Jackson Laboratory	Cat# 010908; RRID: IMSR_JAX:010908
B6.Cg-Npy ^{tm1(cre)Zman/J}	The Jackson Laboratory	Cat# 027851; RRID: IMSR_JAX:027851
Software and algorithms		
MATLAB	MathWorks	R2020b
R	The R Foundation for Statistical Computing	R version 4.0.3

RESOURCE AVAILABILITY

Lead contact

Requests for further information and resources should be directed to the lead contact, J.J.L. (johannes.letzkus@physiologie.uni-freiburg.de).

Materials availability

This study did not generate new unique reagents. All mouse lines, AAVs, and reagents used in this study can be commercially acquired from the respective supplier (see [key resources table](#) for reference).

Data and code availability

- All data related to Figures 1, 2, 4, 5, and 6, electrophysiological data related to Figure 3, and all custom analysis code are deposited at [zenodo.org](https://doi.org/10.5281/zenodo.10938947) (<https://doi.org/10.5281/zenodo.10938947>). Histological data related to Figure 3 is deposited in separate repositories (<https://doi.org/10.5281/zenodo.10938467> and <https://doi.org/10.5281/zenodo.10938471>).
- All custom analysis code used for data analysis and statistics is additionally deposited on GitHub for easier accessibility (<https://github.com/janH-21/NDNF-interneurons-cortical-circuits/>).
- Any additional information required to reanalyze the data reported in this paper is available from the [lead contact](#) upon request.

METHOD DETAILS

Animal subjects

Mice of both sexes (age 78–242 days, median 125) were used in this study, and all mouse lines used were maintained on a C57BL6/J background. Mice were housed under a 12h light/dark cycle and provided with food and water *ad libitum*. After surgical procedures, mice were individually housed. All animal procedures were executed in accordance with institutional guidelines, and approved by the prescribed authorities (Regierungspräsidium Darmstadt and Freiburg).

Surgery

Mice were anesthetized with isoflurane (induction: 4%, maintenance: 1.5–2%) in oxygen-enriched air (Oxymat 3, Weinmann, Hamburg, Germany) and fixed in a stereotaxic frame (Kopf Instruments, Tujunga, USA). Core body temperature was maintained at 37.5°C via a feedback controlled heating pad (FHC, Bowdoinham, ME, USA). Analgesia was provided by local injection of ropivacaine under the scalp (16.7 mg/kg, Ropivacaine-HCl B. Braun) and subcutaneous injection for systemic action of metamizol (200 mg/kg, Novaminsulfon-ratiopharm) and meloxicam (1–2 mg/kg, Metacam Boehringer Ingelheim). Adeno-associated viral vectors (AAV, serotype 2/1, 2/5 or 2/9, max. 700nL) were injected from glass pipettes connected to a pressure ejection system (PDES-02DELA-2, NPI, Germany) into auditory cortex at the following coordinates: 2.46 mm posterior from bregma, 4.6 mm lateral of midline, depth below cortical surface 100–600µm.

Slice preparation

Mice of both sexes (age 78–242 days, median 125) were deeply anesthetized with isoflurane (5%) in oxygen-enriched air (Oxymat 3, Weinmann, Hamburg, Germany), and decapitated into carbonated, ice-cold slicing solution. A Leica VT 1200S vibratome was used to obtain 350µm thick coronal slices from auditory cortex. Slices were directly transferred to carbogenated slicing solution at 33°C for 10min, and then further transferred to carbogenated standard ACSF at room temperature. After 30–60 min recovery time, slices were used in whole-cell patch-clamp experiments. Slicing solution contained (in mM) 93 NMDG, 93 HCl, 2.5 KCl, 1.2 NaH₂PO₄, 30 NaHCO₃, 20 HEPES, 25 glucose, 5 sodium ascorbate, 2 thiourea, 3 sodium pyruvate, 10 MgSO₄ and 0.5 CaCl₂ and was calibrated to a pH of 7.3–7.4 and an osmolality of 300–310mOsm. Standard ACSF contained (in mM) 125 NaCl, 3 KCl, 1.25 NaH₂PO₄, 26 NaHCO₃, 10 glucose, 1 MgCl₂ and 2 CaCl₂ and was calibrated to an osmolality of 300–310mOsm.

Patch clamp electrophysiology

Slices were held in a recording chamber at 33°C and perfused with ACSF (2–4 mL/min). Cells were visualized for patching using differential interference contrast microscopy (Scientifica) or under epifluorescence for identification using an LED (488 or 565 nm, Cool LED) with a water immersion objective (Olympus LUMPlanFLN40xW) and a CCD camera (Scientifica SciCam Pro). Cells were recorded in whole-cell patch-clamp recordings using pipettes pulled from standard-wall borosilicate capillaries using a DMZ Zeitz-Puller to 3.5–6 MOhm resistances. Intracellular solution contained (in mM): 140 K-gluconate, 10 KCl, 10 HEPES, 4 Naphosphocreatine, 4 ATP-Mg, 0.4 GTP and biocytin (4 mg/mL) and was calibrated to pH 7.3 with KOH and an osmolality of 290–300 mOsm. A Multiclamp 700B amplifier (Axon Instruments, CA) was used for whole-cell voltage clamp or current clamp recordings, together with a Digidata1550 (Molecular Devices) for digitization. Recordings were low pass filtered at a 10kHz using a Bessel filter and digitized at 50kHz. Series resistance was routinely compensated in voltage clamp and recordings were excluded if access resistance exceeded 30MOhm.

Intrinsic electrophysiological properties

NDNF L1INs were identified genetically by expressing AAV2/5.EF1a.DIO.hChR2(H134R)-EYFP.WPRE.hGH (PennVector Core) in *Ndnf*-ires-cre-ERT2 animals (B6(Cg)-*Ndnf*^{tm1.1(cre/ERT2)spgl}/J, The Jackson Laboratory), by expressing AAV2/1-EF1a-fDIO-EYFP-WPRE (UNC Vector Core) in *Ndnf*-ires-FlpO animals (B6(Cg)-*Ndnf*^{tm1.1(flpO)spgl}/J, The Jackson Laboratory) or by crossing *Ndnf*-ires-cre-ERT2 animals with an ai9 tdTomato reporter line (B6.Cg-Gt(ROSA)26Sor^{tm9(CAG-tdTomato)Hze}/J, The Jackson Laboratory). Intersectional NDNF/NPY L1INs were identified by crossing *Ndnf*-ires-FlpO mice with *Npy*-cre (B6.Cg-*Npy*^{tm1(cre)Zman}/J, The Jackson Laboratory) mice and expressing AAV2/5-hSyn-Con/Fon EYFP-WPRE (UNC Vector Core) or AAV2/5-hSyn-Con/Fon-hChR2(H134R)-EYFP-WPRE (UNC Vector Core). Intrinsic properties were recorded in current clamp at the cells spontaneous resting membrane potential using a protocol consisting of 1 s baseline without any current injection, a 1 s current injection step, and 2 s baseline. Current steps started at –100pA or –40pA and increased by 10pA every sweep. Cells were included for analysis if they met general recording quality criteria and all intrinsic properties could be estimated.

Connectivity

For optogenetic probing of connectivity from NDNF L1INs to VIPINs, *Ndnf-ires-FlpO* mice were crossed with VIP-cre mice (STOCK *Vip^{tm1(cre)Zjh}/J*, The Jackson Laboratory). AAV2/1-EF1a-fDIO-ChrimsonR-wpre-sv40 (Vector Biolabs) and AAV2/1-EF1a-fDIO-EYFP-WPRE (UNC Vector Core) were used for identification and optogenetic activation of NDNF L1INs, and AAV2/1.CAG.Flex.tdTomato.WPRE.bGH (PennVector Core) was used for identification of VIPINs. For probing connectivity from NDNF L1INs to PCs and PV and non-FS INs, AAV2/5.EF1a.DIO.hChR2(H134R)-EYFP.WPRE.hGH (PennVector Core) was used in *Ndnf-ires-cre-ERT2* animals for identification and optogenetic activation of NDNF L1INs, and pAAV-mDLX-NLS-mRuby (addgene) or pAAV-S5E2-Gq-P2A-dTomato (addgene) were used to aid identification of INs in general for PVINs in particular. Pyramidal cells were identified morphologically. Interneurons identified by pAAV-mDLX-NLS-mRuby with a maximum evoked firing rate >150Hz were counted as PVINs. For probing connectivity from NDNF/NPY L1INs to L2/3INs, *Ndnf-ires-FlpO* animals were crossed with *Npy-cre* animals and AAV2/5-hSyn-Con/Fon-hChR2(H134R)-EYFP-WPRE was used to identify and optogenetically activate NDNF/NPY L1INs. L2/3 pyramidal cells and PV and non-FS INs were identified in the same manner as in *Ndnf-ires-cre-ERT2* animals described above. Calibration experiments were conducted for all optogenetic activators used in order to determine a LED power eliciting approximately one action potential per 0.5ms LED pulse in the NDNF or NDNF/NPY L1IN population, by recording NDNF or NDNF/NPY L1INs in current clamp and applying the same protocol as for actual connectivity recordings (see below). Connectivity was probed in VC with recorded cells clamped to -50mV by delivering a train of four 0.5ms LED pulses at 1Hz for 10–15 sweeps (Figures 1 and 3), and a train of 5ms pulses at 50Hz (Figure 6) at the calibrated LED power. Recordings with a negative holding current at -50mV were excluded as we assumed poor cell health. Light was delivered in full-field application through the objective, using a LED (Cool LED) at 488nm (for ChR2) or 565nm (for ChrimsonR). For offline processing, signals were averaged across sweeps and filtered with a 4-pole Butterworth filter with a F_c of 500Hz. Cells were considered connected if the average signal after the first LED pulse exceeded the third standard deviation of the pre-LED pulse baseline. Only the first IPSC in every train was used for analysis of IPSC characteristics. IPSCs with amplitudes <10pA were excluded from the analysis of IPSC kinetics due to low SNR. Amplitude was calculated as the difference between the pre-LED baseline and the maximum value of an IPSC. Charge was calculated as the integral over 1 s after the LED stimulus. Latency to peak was calculated as time between LED onset and IPSC maximum value. Rise time was calculated as times between the points at which the signal crossed 20% and 80% of the amplitude on the signal upstroke. Decay time was calculated as time between the points at which the signal crossed 80% and 20% of the amplitude on the signal downstroke. GABA-B contributions were measured by application of $3\mu\text{M}$ CGP-55845 and comparison of pre and post CGP application IPSC decay times. Recordings were excluded if access resistance differed by more than 20% between pre and post CGP recordings.

Persistent firing

Persistent firing in NDNF L1INs was investigated using the same recordings as for intrinsic electrophysiological properties. Persistent firing was also investigated in NDNF/NPY L1INs as well as all L2/3 cell types included in analysis of connectivity, following the same protocol as in NDNF L1INs (although in a fraction of cells, current step amplitude increased by 20pA with every sweep). For all recordings using the 1-s current step protocol, only recordings were considered for analysis of persistent firing if cells reached depolarization block at the end of the recording, in order to prevent biasing the rates of occurrence by recordings which might have been terminated too early. To test the effect of synaptic blockers on persistent firing in NDNF L1INs, blockers were bath-applied and cells were incubated for 10–30min prior to recording. In addition, in genetically identified NDNF L1INs, persistent firing was investigated using a protocol consisting of 250ms current injections steps at 2Hz, with 19 steps per sweeps and 10 sweeps. In this protocol, injected current amplitudes were constant and calibrated to elicit action potentials at approximately 28Hz during the first step.

Fluorescent *in situ* hybridization (FISH)

Ndnf-FlpO::NPY-Cre mice were injected with AAV2/5-hSyn-Con/Fon-EYFP-WPRE (UNC) in ACx. 6 weeks post-injection, mice were anesthetized with isoflurane, sacrificed and the brains were then dissected, embedded in Tissue-Tek O.C.T. compound (Sakura) and frozen in isopentane at -55 to -60°C . $16\mu\text{m}$ -thick sections from these fresh frozen brains were prepared using a cryostat (Leica) and mounted on SuperFrost Plus microscope slides (Thermo Scientific). Sections were screened for fluorescence in ACx (Zeiss Axio Zoom) and then stored at -80°C until FISH was performed using the RNAscope Fluorescent Multiplex Reagent Kit (#320850, Advanced Cell Diagnostics). Heating steps were performed using the HybEZTM oven (Advanced Cell Diagnostics). Tissue sections were treated with pretreatment solutions and then incubated with RNAscope probes (Mm-Npy-C2, #313321-C2; Mm-Ndnf-C3, #447471-C3) diluted in probe diluent (#300041), followed by amplifying hybridization processes. This was followed by immunofluorescent staining of EYFP. Blocking solution consisted of 10% normal goat serum and 0.5% Triton in PBS-0.2% gelatin. Primary antibody chicken anti-GFP (Aves) was diluted in 5% normal goat serum and 0.5% Triton in PBS-0.2% gelatin. DAPI was used as a nuclear stain. Prolong Gold Antifade (Thermo Scientific) was used to mount slides. Images were acquired on a confocal microscope (Zeiss LSM 880). EYFP-expressing cells, their distance from the pia and overlap with markers were quantified using a custom written MATLAB (MathWorks) script. The sensitivity is the probability to detect a signal (EYFP) when there actually is a signal, and was calculated as number of true positives/(number of true positives + number of false negatives). True positives are cells labeled by EYFP and both, *Ndnf* and *Npy* mRNA. False negatives are cells that are labeled by both mRNAs but not by EYFP. The specificity is the

probability not to detect a signal when there is no signal, and was calculated as number of true negatives/(number of true negatives + number of false positives). True negatives are cells not labeled by EYFP and labeled by only one, *Ndnf* or *Npy* mRNA. False positives are cells labeled by EYFP and maximally one mRNA.

QUANTIFICATION AND STATISTICAL ANALYSIS

All statistical analyses were done using MATLAB. For clustering analyses, each intrinsic property from NDNF and NDNF/NPY L1INs was normalized to a range between 0 and 1. Data from NDNF and NDNF/NPY L1INs was normalized together to ensure comparability. For unsupervised clustering, Ward's method was used using normalized data from NDNF L1INs. PCA was calculated using normalized data from NDNF L1INs. Comparison with data from NDNF/NPY L1INs was done by projecting normalized NDNF/NPY L1IN intrinsic properties into PC space using PCA coefficients obtained from calculating PCA on NDNF L1IN data. All data was tested for normality before statistical testing using the one-sample Kolmogorov-Smirnov test, a Lilliefors test, Jarque-Bera test and Anderson-Darling test. If all test indicated a normal distribution, parametric methods were used, and non-parametric methods otherwise. In addition, datasets containing both normal and non-normal distributed data were analyzed using only non-parametric methods for comparability. For parametric test, a paired t test was used for paired comparisons with two samples. For non-parametric tests, the Kruskal-Wallis test was used for group-wise between group comparisons, and the Friedman test for group-wise within-group comparisons. If they proved significant at alpha of 0.05, they were followed by the Dunn-Šidák procedure for pairwise testing and multiple test correction. Non-parametric, non-paired comparisons between two samples were done using Wilcoxon's rank-sum test. Non-parametric, paired comparisons between two samples were done using Wilcoxon's signed rank test. Boxplots indicate median (central line), 25th and 75th percentile (box), the most extreme data point within 1.5 times the interquartile range (whiskers), and outliers beyond the whiskers (red crosses). Outliers were always included in statistical analyses. Statistics indicated in plots read as: n.s. $p \geq 0.05$, * $p < 0.05$, ** $p < 0.01$, *** $p < 0.001$.

Cell Reports, Volume 43

Supplemental information

**Layer 1 NDNF interneurons are specialized
top-down master regulators of cortical circuits**

Jan Hartung, Anna Schroeder, Rodrigo Alejandro Pérez Vázquez, Rogier B. Poorthuis, and Johannes J. Letzkus

Supplementary information

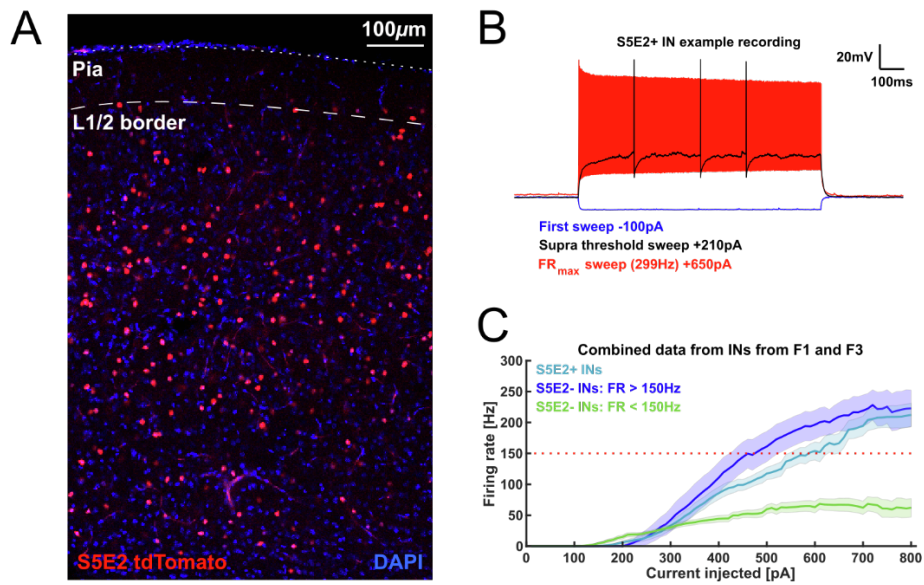


Figure S1. S5E2 labels cortical fast-spiking PV INs. Related to Figure 1. (A) Example histology of pAAV-S5E2-Gq-P2A-dTomato. tdTomato expression is absent from cortical L1, consistent with the distribution of PV expression in mouse auditory cortex¹⁶. Single confocal plane using a 20x objective, scale bar indicates 100μm. (B) Example firing pattern of a L2/3 PVIN identified by S5E2 expression. (C) I-O plot of PV and non-FSIN sustained firing rates in response to a 1-second current injection. $n_{S5E2+}=34$, $n_{S5E2-, >150Hz}=9$, $n_{S5E2-, <150Hz}=27$. The plot includes data from all INs recorded in F1 and F3 except for genetically identified VIPINs.

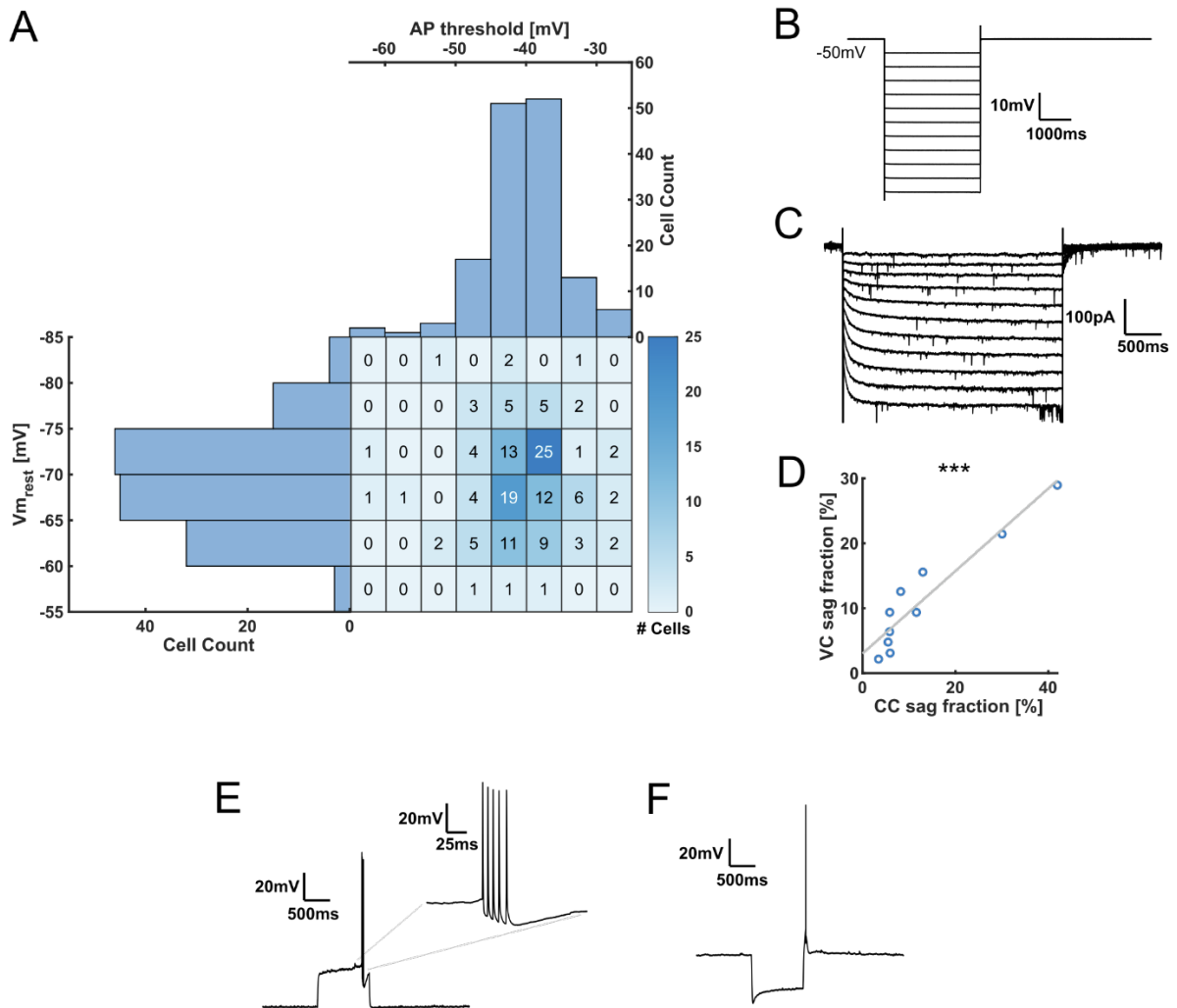


Figure S2. Quality control of electrophysiological recordings in NDNF L1INs. Related to Figure 2. (A) Marginal distribution of NDNF L1IN AP threshold and resting membrane potential. (B) Protocol for measuring sag currents in voltage clamp. Cells were clamped to -50mV and hyperpolarized with voltage steps increasing by -5mV each sweep, up to a maximum hyperpolarization of -105mV. (C) Example recording of the voltage clamp sag fraction protocol in a NDNF L1IN. (D) Correlation of sag fractions measured in voltage clamp and current clamp ($n_{cells}=10$). Pearson correlation coefficient $R=0.94$, $p=4.1e-5$. (E) Burst firing upon spike onset was rarely observed in late-spiking NDNF or NDNF/NPY L1INs (2/166 NDNF L1INs and 1/39 NDNF/NPY L1INs). These cells were excluded from analysis of intrinsic properties. (F) Rebound spikes were observed rarely after hyperpolarization of NDNF L1INs with large voltage sag (3/166 NDNF L1INs).

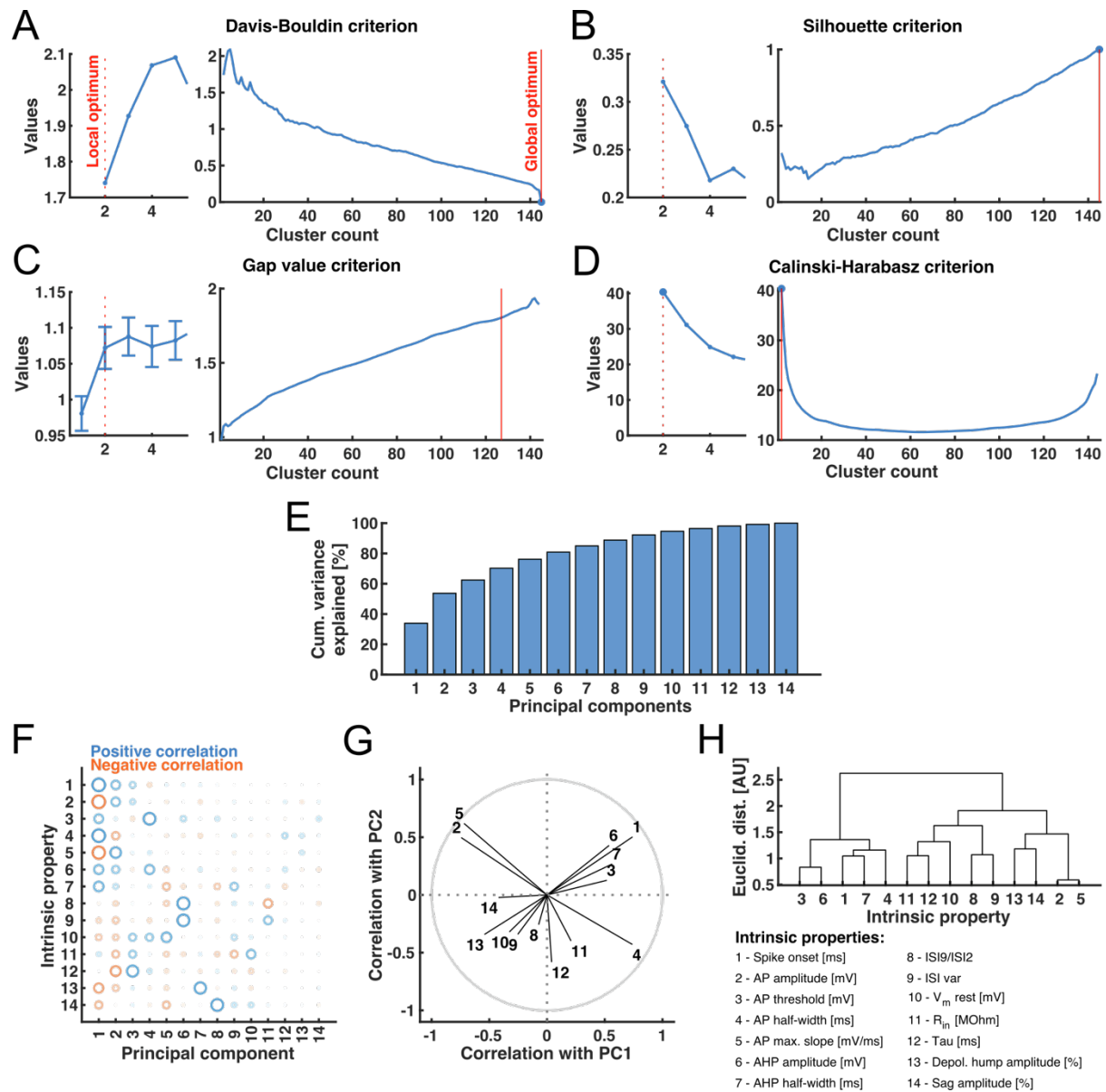


Figure S3. Cluster validation and relation to intrinsic electrophysiological properties. Related to Figure 2. (A)-(D) Validation of Ward's unsupervised clustering using Davis-Bouldin (A), Silhouette (B), Gap value (C), and Calinski-Harabasz (D) criteria. Left plots focus on 1 to 5 clusters, dotted red lines indicate local optima. Right plots show full distributions, solid red lines indicate global optima. All 4 criteria identify 2 clusters as local optimum number, whereas global maxima vary. (E) Cumulative variance explained by PCs calculated from NDNF L1IN intrinsic properties. (F) Contribution of intrinsic properties to PCs measured by their correlation of intrinsic properties with PCs. Circle size indicates correlation strength, circle colors indicate direction of correlation. Absolute correlation strength indicates amount of contribution of a property to a PC. (G) Correlation of intrinsic properties with first two PCs. Grey unity circle indicates maximum correlation. Magnitude of vectors indicates contribution of a property to first two PCs and thus relevance for clustering. Vectors pointing into similar directions indicate that properties typically occur positively correlated within a given NDNF L1IN, vectors pointing into opposite directions indicate that properties typically occur anticorrelated. (H) Ward's unsupervised clustering of correlation coefficients between all intrinsic properties and all PCs. Short distances

39 between intrinsic properties indicate that they typically occur correlated in a given NDNF L1IN, long
40 distances that they typically occur anticorrelated.
41

A

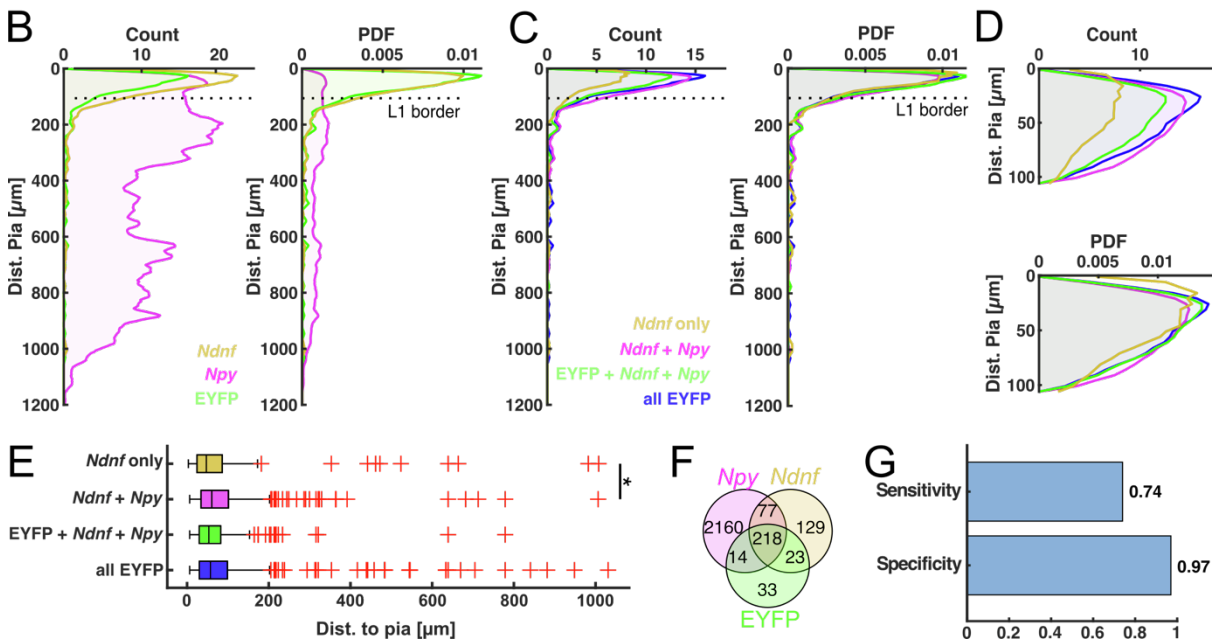
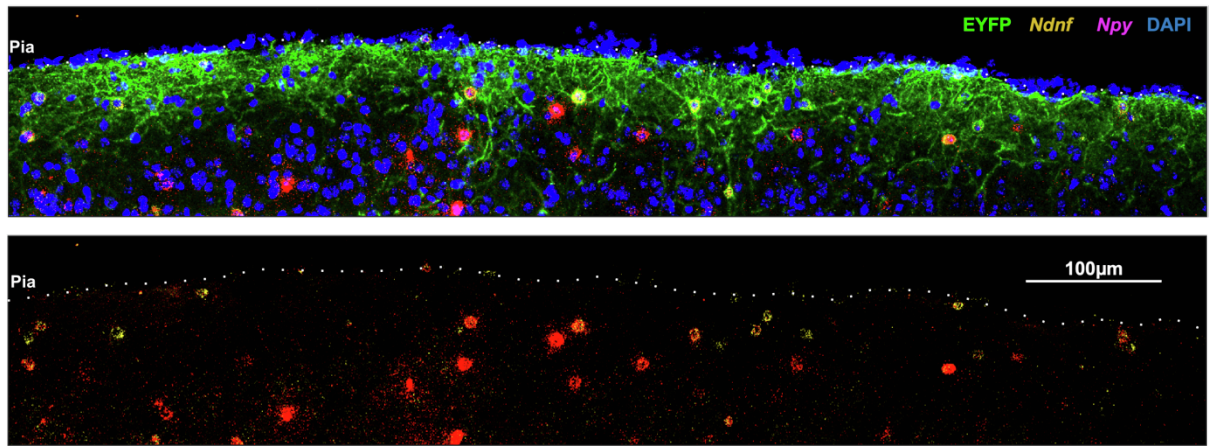


Figure S4. Intersectional genetic targeting of NDNF/NPY L1INs using Boolean logic recombinase approach. Related to Figure 3. (A) Larger example histology of the validation experiment. Scale bar indicates 100µm. (B) Depth profile of used makers, bin width = 5µm. Yellow: all *Ndnf* expressing cells (n=447), Magenta: all *Npy* expressing cells (n=2469), green: all EYFP expressing cells (n=288). (C) Depth profile of combinations of interest for validation, bin width = 5µm. Yellow: cells labeled for *Ndnf* but not *Npy* mRNA (n=152), magenta: cells labeled for *Ndnf* and *Npy* mRNA (n=295), green: cell labeled for both mRNAs and expressing EYFP (n=218), blue: all cells expressing EYFP (n=288). (D) Same as C, but only considering the first 100µm below the pia. (E) Statistical quantification of C. Kruskal-Wallis test with post-hoc Dunn's procedure: $p_{\text{group}}=0.015$. $p_{\text{Ndnf-Ndnf/Npy}}=0.016$, $p_{\text{Ndnf-EYFP}}=0.85$, $p_{\text{Ndnf-allEYFP}}=0.15$, $p_{\text{Ndnf/Npy-EYFP}}=0.22$, $p_{\text{Ndnf/Npy-allEYFP}}=0.92$, $p_{\text{EYFP-allEYFP}}=0.81$. We observe a slight difference in cortical depth between NPY+ and NPY- NDNF L1INs, but do not find a similar difference between the electrophysiologically defined NDNF L1IN clusters (Fig. 2I). (F) Venn diagram displaying the numbers of cells labeled by *in situ* hybridization and/or expressing EYFP (total 2654 cells in 5 mice). (G) Sensitivity and specificity of intersectional targeting calculated using *in situ* hybridization labeling as ground truth. Red crosses in boxplots represent outliers and were included in the analysis.

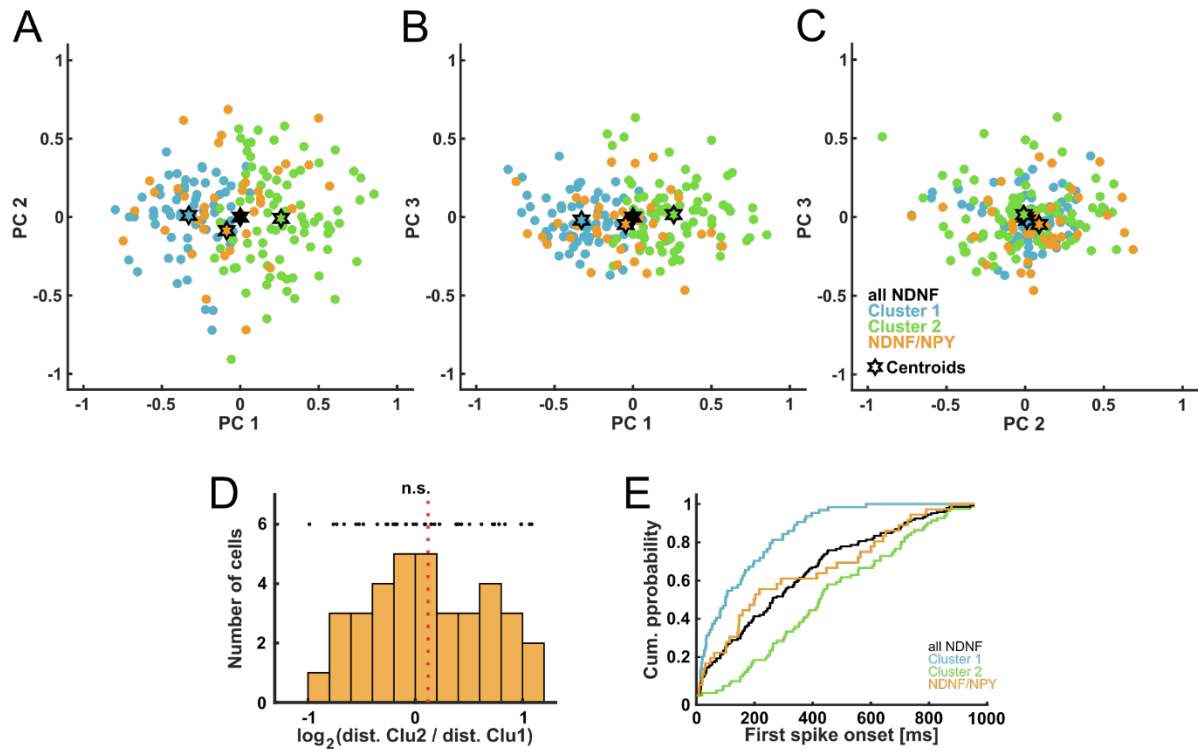


Figure S5. NDNF and NDNF/NPY L1INs have similar electrophysiological properties. Related to Figure 3. (A) – (C) Projection of NDNF/NPY L1INs into NDNF L1IN principal component space based on NDNF/NPY L1IN intrinsic properties and NDNF L1IN PCA coefficients. $n_{\text{Cluster1}}=64$, $n_{\text{Cluster2}}=81$, $n_{\text{NDNF/NPY}}=36$. (D) Histogram of distance ratios of individual NDNF/NPY L1INs to centroids of NDNF L1IN clusters in full intrinsic property space. Data was log-transformed in order to scale distance ratios symmetrically around zero. $n_{\text{NDNF/NPY}}=36$, 1-sample Kolmogorov-Smirnov-test $p=0.11$. Black dots indicate single data points, red line indicates distribution mean at 0.12. (E) Cumulative distribution of spike onset times. $n_{\text{NDNF}}=145$, $n_{\text{Cluster1}}=64$, $n_{\text{Cluster2}}=81$, $n_{\text{NDNF/NPY}}=36$.

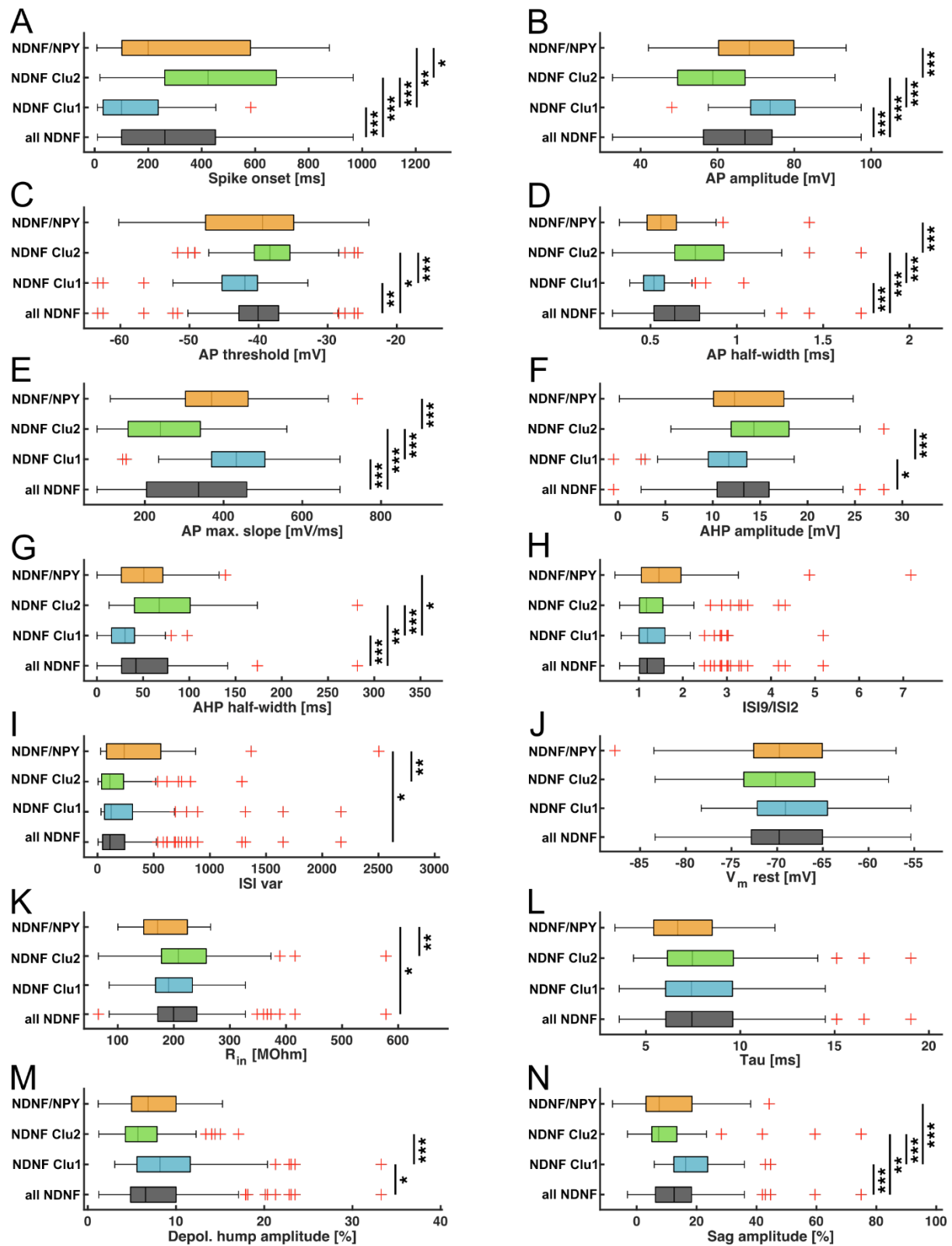


Figure S6. Intrinsic properties by genetic and cluster identity. Related to Figure 3. All statistics done by applying the Kruskal-Wallis-test and post-hoc Dunn's correction for multiple testing. 1 – all NDNF L1INs (n=145), 2 – NDNF Clu1 (n=64), 3 – NDNF Clu2 (n=81), 4 – NDNF/NPY Ins (n=36). (A) Spike onset. $P_{\text{group}}=1.1\text{e-}12$, $p_{12}=1.1\text{e-}5$, $p_{13}=2.8\text{e-}4$, $p_{14}=1$, $p_{23}=1.2\text{e-}13$, $p_{24}=0.0098$, $p_{34}=0.011$. (B) Action potential amplitude. $P_{\text{group}}=3.1\text{e-}5$, $p_{12}=3.1\text{e-}5$, $p_{13}=5.9\text{e-}4$, $p_{14}=0.81$, $p_{23}=1.5\text{e-}12$, $p_{24}=0.14$,

p₃₄=9.2e-4. (C) Action potential threshold. P_{group}=7.8e-7, p₁₂=0.003, p₁₃=0.018, p₁₄=0.81, p₂₃=1.4e-7,
 p₂₄=0.11, p₃₄=0.15. (D) Action potential half-width. P_{group}=9.5e-14, p₁₂=1.5e-5, p₁₃=3.5e-4, p₁₄=0.083,
 p₂₃=2.6e-13, p₂₄=0.79, p₃₄=2.5e-6. (E) Maximum action potential slope. P_{group}=2.1e-12, p₁₂=2.6e-5,
 p₁₃=5.1e-4, p₁₄=0.48, p₂₃=9.5e-13, p₂₄=0.33, p₃₄=1.4e-4. (F) After-hyperpolarization amplitude. P_{group}
 2.9e-5, p₁₂=0.015, p₁₃=0.057, p₁₄=1, p₂₃=7.1e-6, p₂₄=0.25, p₃₄=0.25. (G) After-hyperpolarization half-
 width. P_{group}=4.7e-10, p₁₂=1.3e-4, p₁₃=0.0017, p₁₄=1, p₂₃=5.8e-11, p₂₄=0.014, p₃₄=0.067. (H) Inter-spike
 interval 9 vs. 2 ratio. P_{group}=0.58. (I) Inter-spike interval variance. P_{group}=0.0028, p₁₂=0.67, p₁₃=0.81,
 p₁₄=0.023, p₂₃=0.15, p₂₄=0.51, p₃₄=0.0029. (J) Resting membrane potential. P_{group}=0.58. (K) Input
 resistance. P_{group}=0.0078, p₁₂=0.84, p₁₃=0.92, p₁₄=0.031, p₂₃=0.37, p₂₄=0.43, p₃₄=0.0067. (L)
 Membrane time constant. P_{group}=0.18. (M) Depolarizing hump amplitude. P_{group}=4e-4, p₁₂=0.047,
 p₁₃=0.13, p₁₄=1, p₂₃=1.2e-4, p₂₄=0.4, p₃₄=0.4. (N) Voltage sag amplitude. P_{group}=9e-9, p₁₂=8.9e-4,
 p₁₃=0.0071, p₁₄=0.42, p₂₃=6.7e-9, p₂₄=1.2e-4, p₃₄=0.99. Red crosses in boxplots represent outliers and
 were included in the analysis.

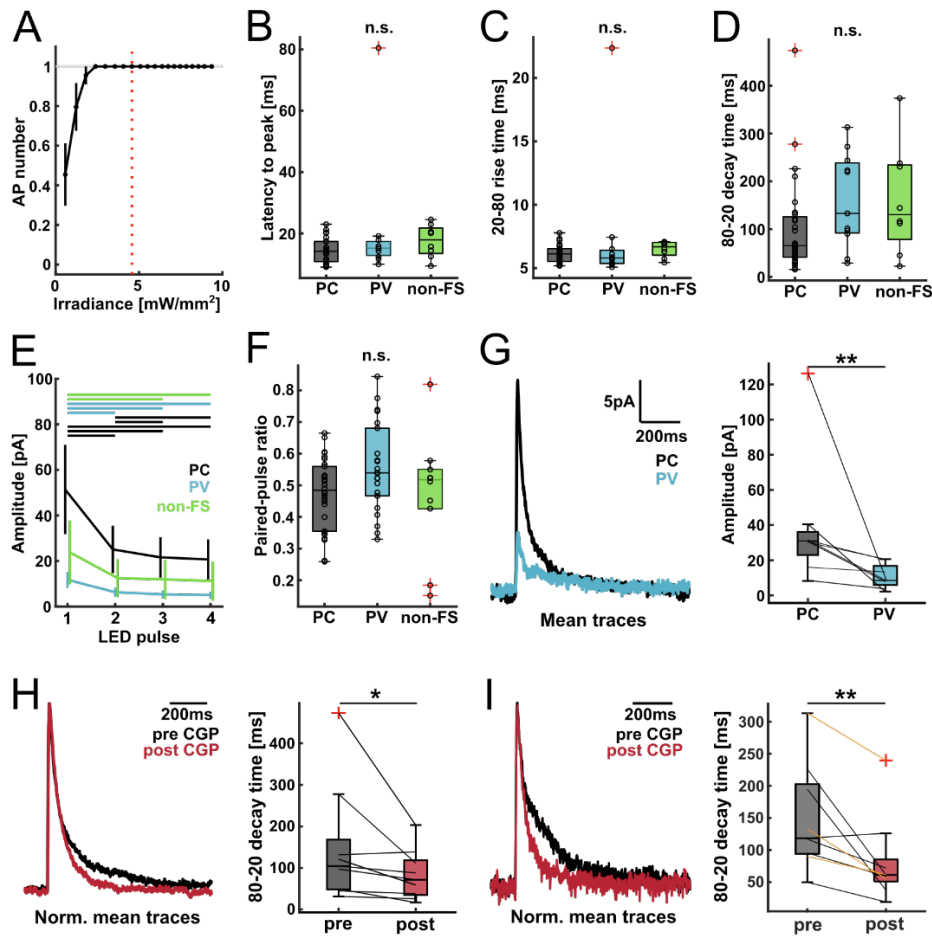


Figure S7. Extended data for NDNF/NPY mediated inhibition of cortical L2/3. Related to Figure 3. (A) Calibration of irradiance to evoke on average one action potential per LED pulse in NDNF/NPY L1INs ($n=11$). Red line indicates chosen irradiance. (B)-(D) NDNF/NPY L1IN-elicited IPSC kinetics ($n_{PC}=28$, $n_{PV}=11$, $n_{nonFS}=8$): latency to peak amplitude (B), 20-80 rise time (C) and 80-20 decay time (D). Kruskal-Wallis-Test: $p_{peak}=0.22$, $p_{rise}=0.2$, $p_{decay}=0.11$. (E) Short-term depression of NDNF/NPY L1IN elicited IPSCs ($n_{PC}=30$, $n_{PV}=22$, $n_{nonFS}=10$). Data displayed as mean \pm SEM. Bars on top indicate significant differences. Within cell type Friedman-Test with post-hoc Dunn's procedure: PC: $p_{group}=6.4e-16$, $p_{12}=0.0019$, $p_{13}=9.3e-10$, $p_{14}=7e-15$, $p_{23}=0.03$, $p_{24}=6.5e-5$, $p_{34}=0.5$. PV: $p_{group}=2.5e-10$, $p_{12}=0.0028$, $p_{13}=3.2e-8$, $p_{14}=7.6e-9$, $p_{23}=0.11$, $p_{24}=0.06$, $p_{34}=1$. non-FS: $p_{group}=8.1e-5$, $p_{12}=0.053$, $p_{13}=0.0041$, $p_{14}=5.4e-4$, $p_{23}=0.97$, $p_{24}=0.34$, $p_{34}=0.88$. (F) Paired-pulse ratio (2nd/1st IPSC amplitude) by cell type ($n_{PC}=30$, $n_{PV}=22$, $n_{nonFS}=10$). Kruskal-Wallis-Test $p=0.15$. (G) Comparison of 'pseudo-paired' inhibition of PCs and PVINs recorded in close proximity by NDNF/NPY L1INs ($n=8$ 'pseudo-pairs'). Left: Average traces. Right: IPSC amplitudes in PCs and PV INs. Wilcoxon signed rank test $p=0.0078$. (H) CGP effect on IPSCs elicited in L2/3 PCs by NDN/NPY L1INs ($n=9$). Left: Average traces. Right: IPSC 80-20 decay times pre- vs. post-CGP. Wilcoxon signed rank test $p=0.02$. (I) CGP effect on IPSCs elicited in L2/3 PVINs by NDNF ($n=6$) and NDNF/NPY L1 ($n=3$) INs. Left: Averaged normalized example traces. Right: Effect of CGP on 80-20 decay times in L2/3 PV INs. Data for NDNF L1IN to PVIN (black lines) and NDNF/NPY L1IN to PVIN (orange lines) connectivity was analyzed together (paired t-test $p=0.0089$). Red crosses in boxplots represent outliers and were included in the analysis.

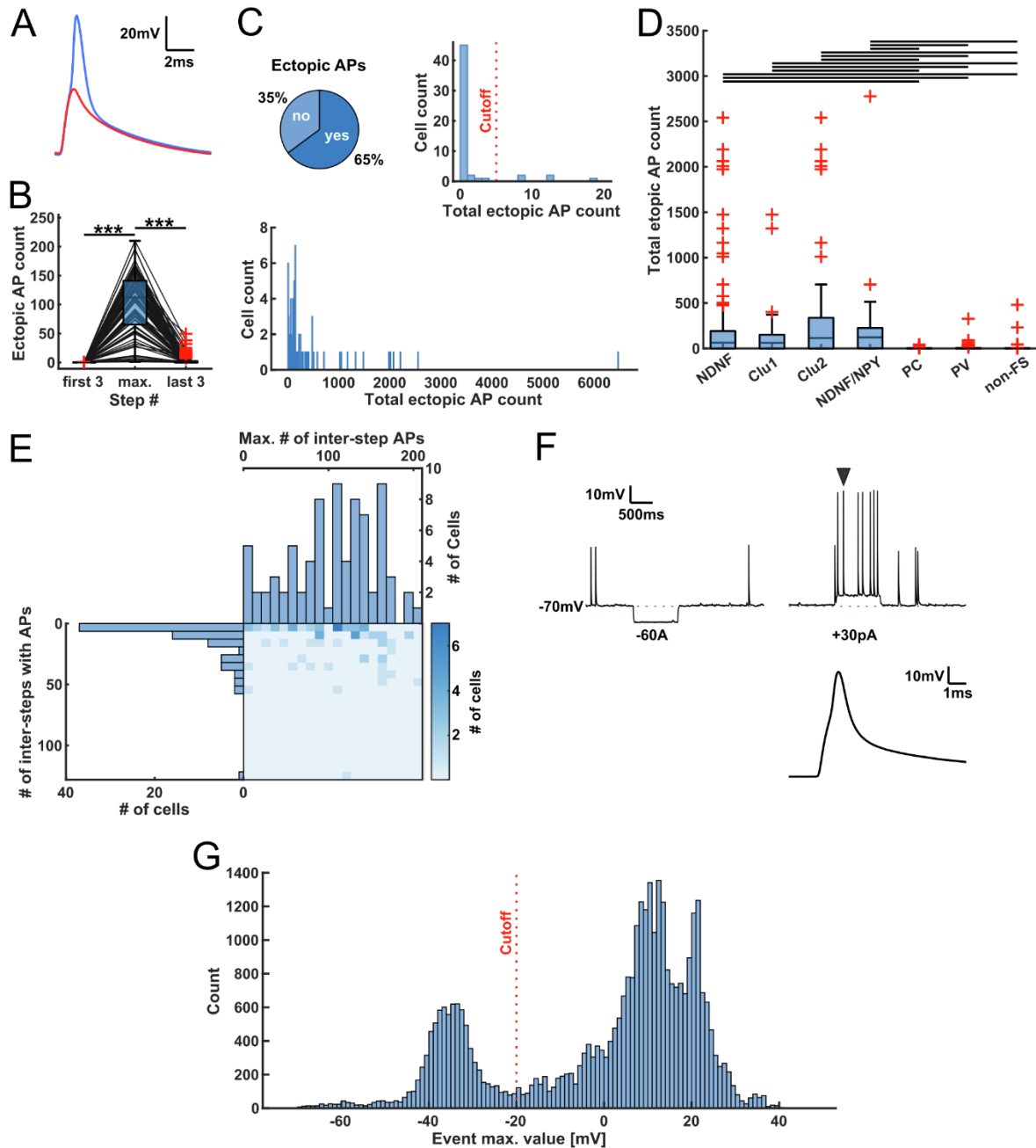
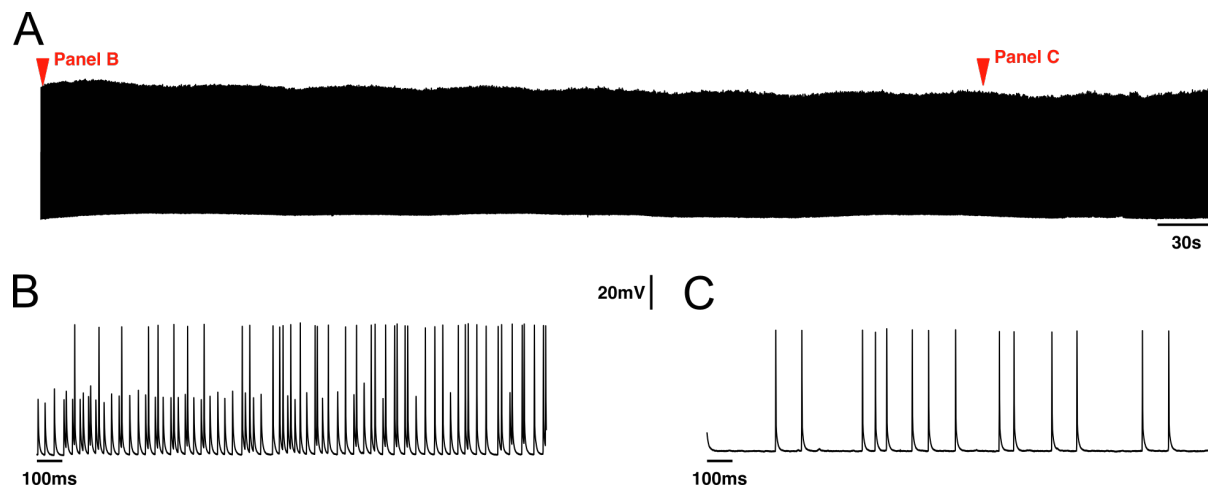


Figure S8. Occurrence of persistent firing. Related to Figure 4. (A) Overlay of persistent firing spike (blue) and spikelet (red), aligned by action potential crossing time. Persistent firing spikes seem to emerge from persistent firing spikelets. Same data as in F4 D and E. (B) Boxplot of number of ectopic events during the first three inter-step intervals with positive current injections, the inter-step interval with the maximum count of ectopic action potentials, and the last three inter-step intervals in each recording ($n=79$ cells with persistent firing). Black lines indicated single data points. Friedman test $p_{\text{group}}=2.8\text{e-}32$ and post-hoc Dunn's procedure $p_{\text{first-max}}=0$, $p_{\text{first-last}}=0.071$, $p_{\text{max-last}}=0$. (C) Upper left: Proportion of NDNF L1INs ($n=128$) that show any ectopic action potentials at all. Upper right: Histogram of total ectopic event count, focused on the first 20 bins (bin width = 1). Red line indicates the cutoff chosen for classifying cells as displaying persistent firing. Lower: Full distribution of total ectopic event count in NDNF L1INs (bin width = 10, cells without ectopic events excluded for display clarity). (D) Total

ectopic event count by cell type ($n_{\text{NDNF}}=128$, $n_{\text{Clu1}}=39$, $n_{\text{Clu2}}=70$, $n_{\text{NDNF/NPY}}=36$, $n_{\text{PC}}=34$, $n_{\text{PV}}=69$, $n_{\text{nonFS}}=44$). Kruskal-Wallis-Test $p_{\text{group}}=4.3\text{e-}16$. Post-hoc Dunn's procedure $p_{\text{NDNF-Clu1}}=1$, $p_{\text{NDNF-Clu2}}=1$, $p_{\text{NDNF-NDNF/NPY}}=1$, $p_{\text{NDNF-PC}}=7.3\text{e-}6$, $p_{\text{NDNF-PV}}=1.5\text{e-}6$, $p_{\text{NDNF-nonFS}}=1\text{e-}5$, $p_{\text{Clu1-Clu2}}=1$, $p_{\text{Clu1-NDNF/NPY}}=0.98$, $p_{\text{Clu1-PC}}=0.003$, $p_{\text{Clu1-PV}}=0.0076$, $p_{\text{Clu1-nonFS}}=0.0071$, $p_{\text{Clu2-NDNF/NPY}}=1$, $p_{\text{Clu2-PC}}=1.8\text{e-}6$, $p_{\text{Clu2-PV}}=6.1\text{e-}7$, $p_{\text{Clu2-nonFS}}=2.8\text{e-}6$, $p_{\text{NDNF/NPY-PC}}=8.3\text{e-}6$, $p_{\text{NDNF/NPY-PV}}=1\text{e-}5$, $p_{\text{NDNF/NPY-nonFS}}=1.7\text{e-}5$, $p_{\text{PC-PV}}=1$, $p_{\text{PC-nonFS}}=1$, $p_{\text{PV-nonFS}}=1$. (E) Marginal distribution of NDNF L1IN ($n=79$) number of inter-step intervals with ectopic action potentials and maximum number of action potentials in an inter-step interval. (F) Example recording of a NDNF L1IN with persistent activity before onset of current-evoked spiking. Upper: Two example sweeps from the same IN with persistent firing spikes and spikelets. Black arrow indicates the action potential on the lower panel with characteristic shoulder. 14 NDNF L1INs showed persistent activity before onset of evoked action potentials. For 12 out of 14, these were typically single spikes. For two neurons, including this example, there was ongoing activity consisting of many events over several sweeps. The latter two cells were excluded from further analysis. (G) Distribution of maximum voltages reached by ectopic action potentials. There are two clear peaks corresponding to full persistent APs and spikelets, respectively (35308 persistent events in 79 cells). The continuity of the distribution between APs and spikelets corresponds to the fact that values vary between cells, and in particular that persistent APs do not always reach the same voltages as current evoked APs (see also Fig. S11A for an example). We chose the voltage at the minimum count between the two peaks (-20mV) as a cutoff to distinguish between pF APs and spikelets, indicated in the plot by the red line. Red crosses in boxplots represent outliers and were included in the analysis.

144



145

146

147

148

149

150

Figure S9. Persistent firing can be very long-lasting. Related to Figure 4. (A) Whole recording of 10 minutes with continuous persistent firing. (B) Beginning and (C) end of the recording. As observed during shorter episodes of persistent firing in current injection protocols, spikelets tend to be more prevalent at the beginning of the episode.

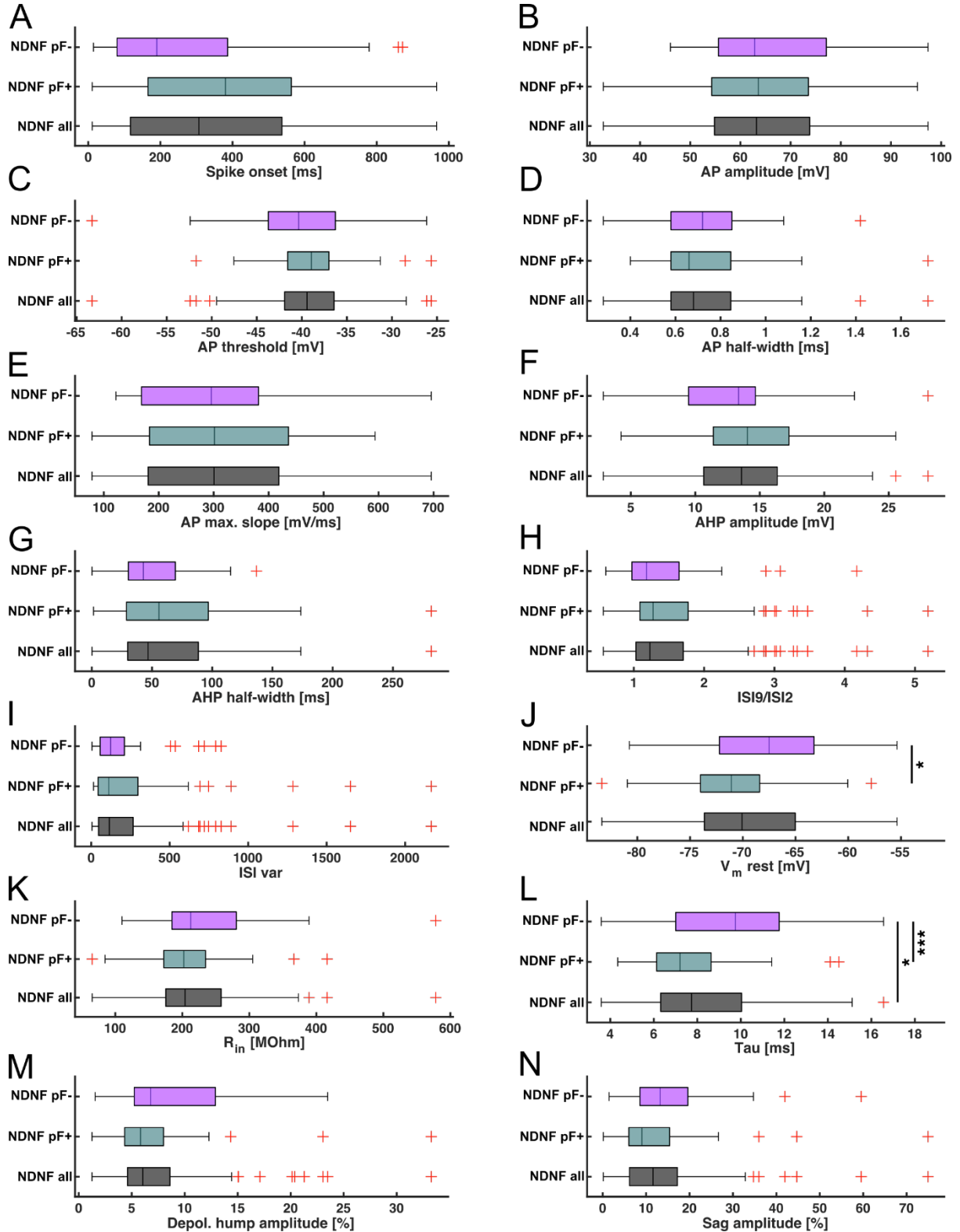


Figure S10. Intrinsic properties of NDNF L1INs by occurrence of persistent firing. Related to Figure 4. All statistics calculated by applying the Kruskal-Wallis-test and post-hoc Dunn's correction for multiple testing. (1) NDNF all: all NDNF L1INs (n=128), (2) NDNF pF+: NDNF L1INs with persistent firing (n=79), (3) NDNF pF-: NDNF L1INs without persistent firing (n=49). (A) Spike onset. $P_{\text{group}}=0.052$. (B) Action potential amplitude. $P_{\text{group}}=0.77$. (C) Action potential threshold. $P_{\text{group}}=0.85$. (D) Action

158 potential half-width. $P_{\text{group}}=1$. (E) Maximum action potential slope. $P_{\text{group}}=0.96$. (F) After-
159 hyperpolarization amplitude. $P_{\text{group}}=0.19$. (G) After-hyperpolarization half-width. $P_{\text{group}}=0.56$. (H) Inter-
160 spike interval 9 vs. 2 ratio. $P_{\text{group}}=0.56$. (I) Inter-spike interval variance. $P_{\text{group}}=0.96$. (J) Resting
161 membrane potential. $P_{\text{group}}=0.024$, $p_{12}=0.48$, $p_{13}=0.18$, $p_{23}=0.019$, (K) Input resistance. $P_{\text{group}}=0.43$. (L)
162 Membrane time constant. $P_{\text{group}}=7.3\text{e-}4$, $p_{12}=0.2$, $p_{13}=0.029$, $p_{23}=4.3\text{e-}4$. (M) Depolarizing hump
163 amplitude. $P_{\text{group}}=0.12$. (N) Voltage sag amplitude. $P_{\text{group}}=0.088$. Red crosses in boxplots represent
164 outliers and were included in the analysis.
165
166

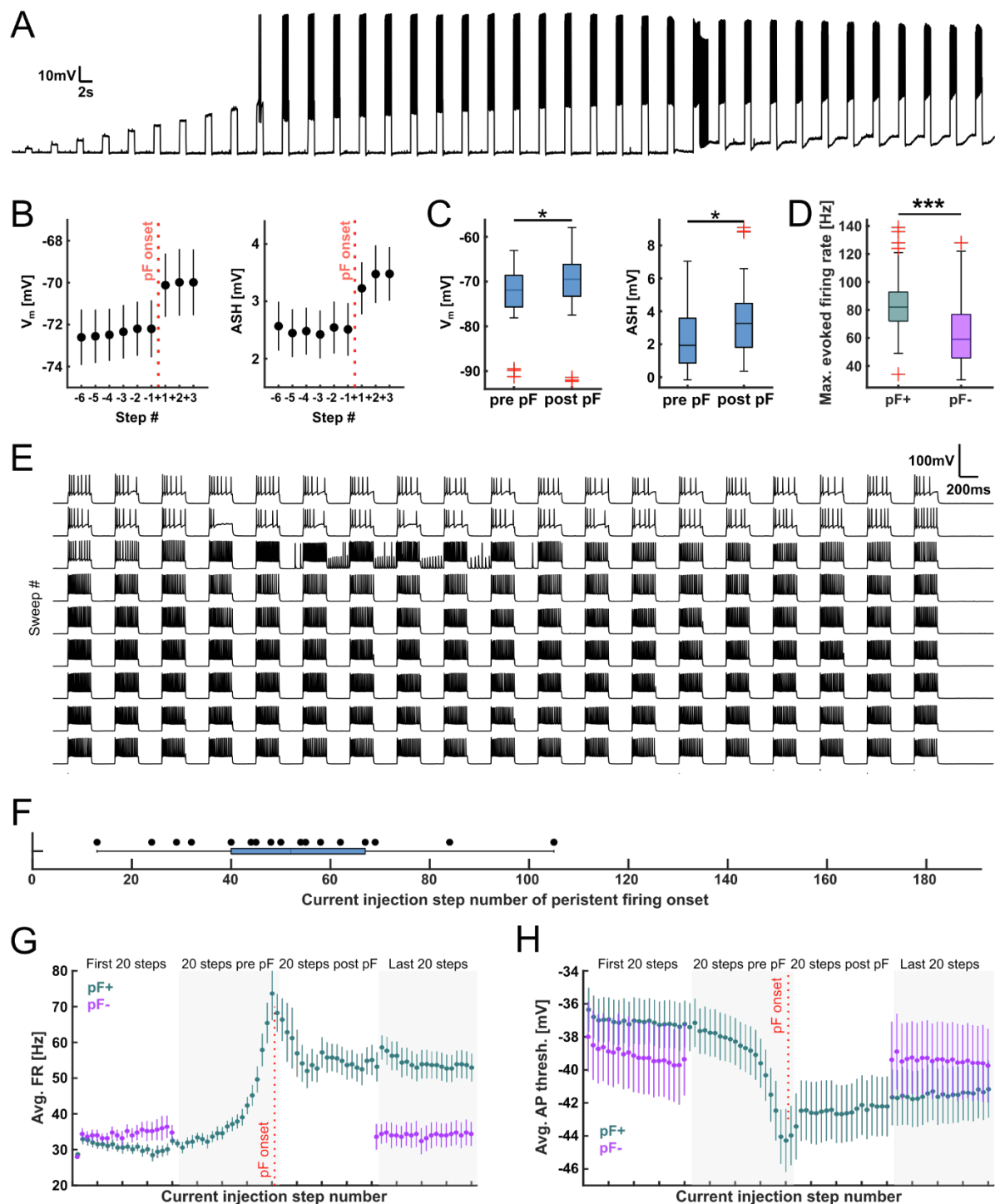


Figure S11. Persistent firing is associated with a state transition in NDNF L1INs. Related to Figure 6.

(A) Example recording highlighting changes in resting membrane potential and after-step hyperpolarization (ASH) after onset of persistent firing. (B) Left: Changes in resting membrane. Right: Changes in ASH. Displayed as mean \pm SEM. Red line indicates persistent firing onset. All recordings of NDNF L1INs were included in which there was no further persistent firing for three inter-step intervals after the initial period ($n=20$ cells). (C) Comparison of the 3 steps preceding vs. the 3 steps following persistent firing onset ($n=20$ cells). Left: Resting membrane potential. Wilcoxon rank sum test $p=0.02$.

Right: ASH. Wilcoxon rank sum test $p=0.015$. (D) Comparison of maximum current-evoked firing rates in Ndnf L1INs that do ($n=79$) or do not ($n=49$) display persistent firing. Wilcoxon rank sum test $p=3e-7$. (E) Complete trace of recording shown in Fig. 6F. (F) Onset step number of persistent firing in NDNF L1INs ($n=18$) using the protocol shown in Fig. 6E. As onset of persistent firing is strongly biased towards the first half of the protocol, absence of persistent firing in the remaining INs is unlikely to be explained by insufficient stimulation. (G) and (H) Extended view of current evoked firing rates in Fig. 6I (G) and action potential thresholds in Fig. 6K (H). In NDNF L1INs which display persistent firing, firing rates and action potential thresholds stay relatively constant at the beginning of the recording. Towards persistent firing onset firing rates rise first slowly and then sharply and peak shortly before persistent firing onset. After the persistent firing period is over, current evoked firing rates fall again, but stay elevated as compared to start of the recording. Similar dynamics are observed for evoked action potential thresholds, but neither evoked firing rates nor action potential thresholds show any dynamics in NDNF L1INs that do not show persistent firing ($n_{pF+}=17$, $n_{pF-}=10$, one NDNF L1IN with persistent firing was not included in (G) and (H) due to onset of persistent firing before the 20th step). Red crosses in boxplots represent outliers and were included in the analysis.

Intrinsic property	Definition [Unit]
First spike onset	Time from onset of current injection to time of threshold of first AP in first step with evoked action potentials. [ms]
Action potential amplitude	Voltage difference between threshold value and maximum AP value. [mV]
Action potential threshold	Voltage value at which AP upstroke crosses 10mV/ms. [mV]
Action potential half-width	Time between AP upstroke and downstroke at the average voltage of threshold and maximum voltage. [ms]
Action potential max. slope	Maximum acceleration on the first temporal derivative of the AP upstroke between time of threshold crossing and time of voltage max. of AP. [mV/ms]
Afterhyperpolarization amplitude	Difference between AP threshold voltage and voltage of first minimum following AP maximum. [mV].
Afterhyperpolarization half-width	Time between AHP downstroke and upstroke at the average voltage of threshold and AHP minimum. [ms]
ISI9/ISI2	Ratio of 9 th and 2 nd inter-spike interval in first sweep with at least 20 APs.
ISI variability	Inter-spike interval variability in first sweep with at least 20 APs.
Resting membrane potential	Median baseline voltage over 1 sec before first current injection. [mV]
Input resistance	Coefficient from linear fit of pre-step baseline voltages and within current step voltages over all passive steps. [MΩ]
Membrane time constant tau	Coefficient from single exponential fit over 50ms starting from current injection in sweep with -40pA current injection. [ms]
Depol. hump amplitude	Relative difference between voltage difference from pre-step baseline to maximum in first 300ms of current step and voltage difference from pre-step to detrended step median in last passive step. [%]
Sag amplitude	Relative difference between voltage difference from pre-step baseline to minimum in first 300ms of current step and voltage difference from pre-step to step median in last step with step voltages lower or equal -75mV. [%]

Table S1. Definition of intrinsic electrophysiological properties. Related to Figure 2. AP and AHP properties (properties 2-7 in the table) were measured in first step with current evoked action potentials and averaged across all APs in that step.